Advanced Methods in Post Cartesian Imaging

by

Ajit Devaraj

A Dissertation Presented in Partial Fulfillment
of the Requirements for the Degree
Doctor of Philosophy

ARIZONA STATE UNIVERSITY

December 2010

Advanced Methods in Post Cartesian Imaging

by

Ajit Devaraj

has been approved

October 2010

Graduate Supervisory Committee:

James G. Pipe, Co-Chair
Lina J. Karam, Co-Chair
David H. Frakes
James T. Aberle

ACCEPTED BY THE GRADUATE COLLEGE

ABSTRACT

Magnetic resonance (MR) imaging with data acquisition on a non-rectangular grid permits a variety of approaches to cover k-space. This flexibility can be exploited to achieve clinically relevant characteristics – fast yet full coverage for short scan times, center out schemes for short T_e, over-sampled k-space for robustness to motion, long acquisition time for improved signal-to-noise (SNR) performance and benign under-sampling (aliasing) artifact.

This dissertation presents advances in Periodically Rotated Overlapping ParallEL Lines with Enhanced Reconstruction (PROPELLER) trajectory design and improved reconstruction for spiral imaging.

Scan time in PROPELLER imaging can be reduced by tailoring the trajectory to the required Field-Of-View (FOV). A technique to design the PROPELLER trajectory for an elliptical FOV is described. The proposed solution is a set of empirically derived closed form equations that preserve the standard PROPELLER geometry and specify the minimum number of blades necessary.

Reconstructing spiral scans requires accurate trajectory information. A simple method to measure the deviation from the designed trajectory due to gradient coupling is presented. A line phantom is used to force a uniform structure in a predetermined orientation in k-space. This uniformity permits measurements of zeroth order trajectory deviations due to gradient coupling.

Spiral reconstruction is also sensitive to B_0 inhomogeneities (variations in the external magnetic field). This sensitivity manifests itself as a spatially varying blur.

An algorithm to correct for concomitant field and first order B_0 inhomogeneity effects is developed based on de-blurring via convolution by separable kernels. To reduce computation time, an empirical equation for sufficient kernel length is derived. It is also necessary to know the noise characteristics of the proposed algorithm; this is investigated via Monte-Carlo simulations. The algorithm is further extended to correct for concomitant field artifacts by modeling these artifacts as blurring due to a temporally static field map. This approach has the potential for further reduction in computational cost by combining the B_0 map with the concomitant field map to simultaneously correct for artifacts resulting from both field inhomogeneities and concomitant field map.

To my mother

ACKNOWLEDGEMENTS

I have only the deepest gratitude towards my wife, parents, sister and brother-in-law for graciously pausing their lives to let me pursue my dream. This dissertation would not have been without their love and encouragement.

My advisor Jim Pipe has been a source of immense support and guidance throughout my doctoral work. He has always been available for an intellectual dialogue on research even a discussion of the latest sci-fi flick. I would not have gone far without his patient tutelage.

I have been fortunate to have Professor Lina Karam as a further source of expert advice during my stay at Arizona State University. She has been kind enough to take an active interest in my work. Conversations with her have helped clarify and extend my thoughts.

I am indebted to Professors David Frakes and James Aberle for making time to serve on my Ph. D. committee. Their feedback has only served to enhance this work.

I also thank my colleagues at the Keller Center for Imaging Innovation for assisting me with my innumerable test scans and making my stay there pleasant.

TABLE OF CONTENTS

Page

LIST OF FIGURES

LIST OF TABLES

Chapter 1

INTRODUCTION

Magnetic Resonance Imaging (MRI) is an emission tomography technique used to form accurate images of an object's internal structure non-invasively. Nuclear resonance, the physical phenomenon behind MRI, was discovered independently by two teams led by Felix Bloch (1) and Edward Purcell (2). A technique to form images using this phenomenon was first proposed by Paul Lauterbur in 1973 (3) as zeugmatography. MRI does not require the introduction of any foreign substance for image generation as is the case in other emission tomography techniques like positron emission tomography (PET) and single photon emission computed tomography (SPECT). Unlike other forms of tomography like transmission (X-Ray) and diffraction tomography (Ultra-Sound), MRI is not dependent on an external signal source to interrogate the object being examined. These characteristics make MRI a powerful tool for the medical community.

MR imaging is generally cartesian, i.e., data is acquired on a traditional rectangular raster. Non-cartesian MR imaging offer vital advantages like fast acquisition (spiral imaging), motion correction (PROPELLER imaging) and ultra short T_e (radial imaging). Non-cartesian imaging has its share of constraints – the trajectory design is non-trivial, gradient sets are required to operate with tighter tolerances, artifacts are normally severe (cannot be "read through"); both reconstruction and arti-

fact correction algorithms are computationally intensive. This thesis presents some work that is expected to make non-cartesian MR imaging more functional. The conducted work contributes to the areas of elliptical field-of-view PROPELLER imaging (Chapter 3), spiral gradient delay correction (Chapter 4) and spiral deblurring (Chapter 5). The contributions, in brief, are:

- PROPELLER is the predominant trajectory for motion corrected 2D imaging. It is usually designed for a circular field-of-view (FOV) and is intrinsically scan time intensive. When imaging oblong objects, savings in scan time can be achieved if the trajectory is designed for an FOV that closely matches the object dimensions. An empirical closed form algorithm to design the PROPELLER trajectory for an elliptical FOV is developed. The trajectory is demonstrated with both phantom and in-vivo imaging. The SNR performance and potential savings in scan time are also presented.

- Gradient delays are a source of substantial artifact in spiral imaging. Algorithms to measure delays usually assume no coupling between gradient sets. A simple experimental setup to measure coupling (if any) between gradient sets is introduced. The results of the experiment on a 3T GE Signa scanner are presented and analyzed.

- Off-resonance during spatial encoding causes a spatially varying blur in spiral imaging. The common causes of field inhomogeneity are B_0 inhomogeneity

and concomitant fields. The spatial variance has traditionally necessitated computationally expensive correction algorithms. A rapid algorithm based on separable de-blur kernels to correct concomitant blur in spiral images is proposed. Details of kernel length requirements, noise performance and extension to account for first-order effects are also presented. The algorithm is validated with results from invivo images. The form of the proposed solution also permits simultaneous B_0 inhomogeneity and concomitant field deblurring.

This thesis is organized as follows. Chapter 2 presents a concise introduction to MRI. Chapter 3 presents the extension of PROPELLER imaging to elliptical FOVs. Chapter 4 presents the work on gradient coupling. Chapter 5 presents extensions to the deblurring algorithm. Chapter 6 summarizes the contributions of this thesis and presents directions for future work.

Chapter 2

MRI: THE BASICS

The application of nuclear magnetic resonance (NMR) as an imaging tool was pioneered by Lauterbur (3). The engineering foundations of MRI as it is known today were laid by Kumar (4) and Mansfield (5). Hardware limitations constrained the diagnostic utility of MR images till the 1980s. With improvements in magnet technology, gradient sets, displays and micro-processors, MRI is now an indispensable diagnostic tool.

This chapter, while giving a brief tour of MRI, serves as an introduction to terms and concepts referred to later. The NMR basis of MRI can be described by either classical electrodynamics or quantum mechanics. For the sake of brevity and since imaging is largely concerned with NMR in liquids (both descriptions are consistent with each other in this regime), the presentation here is largely restricted to the classical description. The interested reader will find that the quantum mechanical picture (6) gives a mathematically rigorous validation for the more geometric (hence more intuitive) portrayal by the classical model.

SPINS

Spin, in the NMR/MRI literature, loosely refers to the atomic nucleus of interest. More explicitly, it refers to the spin quantum number (I) of the atomic nucleus (6).

The total angular momentum (J) of the nucleus is specified by I (6) as:

$$J = \left|\vec{J}\right| = \hbar\sqrt{I(I+1)} \qquad [2.1]$$

Here, $\hbar$ is the Plancks constant for frequency in Hz. By the Weiner-Eckart theorem, the magnitude of the magnetic moment ($\vec{\mu}$) of the nucleus (6) is given by :

$$\mu = |\vec{\mu}| = \gamma J \qquad [2.2]$$

The proportionality constant γ is known as the gyromagnetic ratio. Both I and $\vec{\mu}$ are intrinsic to the nucleus. The actual physical basis for their existence is still not well understood (6). The classical description of MRI adopts an over-simplified notion (7) that the nucleus rotates around an axis giving the angular moment and simultaneously forming the magnetic moment from the revolving electrical charges within the nucleus.

External Magnteic Field

Macroscopic manifestation of $\vec{\mu}$ is in the form of a net/bulk magnetization ($\vec{M}$, the vector sum of $\vec{\mu}$ for all nuclei). Under normal conditions, $\vec{M}$ is zero as the magnetic moments $\vec{\mu}_i$ can be oriented in any direction and can cancel each other. However, in the presence of an external magnetic field (B_0), the component of $\vec{\mu}$ along B_0 (μ_z) is predetermined (7) giving a non-zero $\vec{M}$. The value of μ_z is dictated solely by the value of I (7) :

$$\begin{gathered} \mu_z = \gamma\hbar m_I, \\ m_I = -I, -I+1, \cdots, I, \end{gathered} \qquad [2.3]$$

where m_I is the magnetic quantum number. Since the only permissible values of I are zero, integers and half integers (7), nuclei with $I = 0$ are not MR active. The rest of this thesis is limited to nuclei with $I = 1/2$ as MRI is largely based on these spin $1/2$ systems. It is also fortuitous that the classical model is considerably simplified for the spin $1/2$ systems – μ_z has a set magnitude and is oriented either parallel (spin-up) or anti-parallel (spin-down) with respect to B_0.

By classical mechanics, a magnetic moment in an external magnetic field experiences a torque given by $\vec{\mu} \times \vec{B}$. By definition, a torque is $d\vec{J}/dt$. Using Eq. 2.2 :

$$\frac{d\vec{\mu}}{dt} = \gamma\vec{\mu} \times \vec{B}_0 \qquad [2.4]$$

Solving Eq. 2.4 (7) gives :

$$\mu_{xy}(t) = \mu_{xy}(0)\, e^{-i\gamma B_0 t}, \qquad [2.5]$$

$$\mu_z(t) = \mu_z(0). \qquad [2.6]$$

The motion of μ, as described by Eq. 2.5 and Eq. 2.6, is a precession about the direction of B_0. Figure 2.1 illustrates the precession of a spin with μ_z parallel to B_0. The coordinate system depicted in Fig. 2.1 is stationary and called the laboratory reference frame. By convention, the direction of B_0 is assumed to be along z in the laboratory reference frame. The x-y plane is called the transverse plane. Components of quantities parallel to the x-y plane are referred to as the transverse component (e.g., μ_{xy}, M_{xy}) and components of quantities along z are referred to as

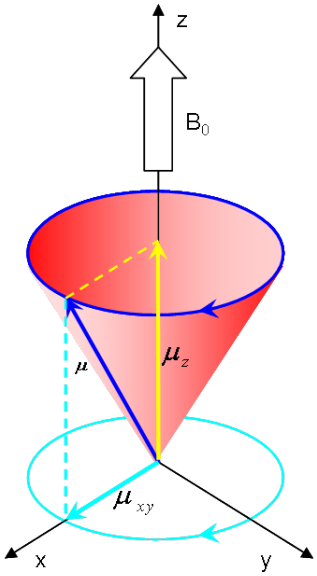

Figure 2.1: Precession of the magnetic moment in the presence of an external magnetic field for a spin $1/2$ nucleus in a spin-up state.

the longitudinal component (e.g., μ_z, M_z). A closer inspection of the exponential term in Eq. 2.5 reveals the frequency of precession as :

$$\omega_0 = \gamma B_0. \qquad [2.7]$$

This relation is the well-known Larmor equation, and the frequency of precession is known as the Larmor frequency. From the Larmor equation, spins experiencing identical external magnetic fields, will have matching Larmor frequencies and are collectively called isochromats.

The choice between spin-up and spin-down states is arbitrary and dynamic – the spins keep migrating between the two states. However, at a given temperature, the total number of spins in either state at any time instant is a constant; this is

referred to as thermal equilibrium (7). At thermal equilibrium, however, the number of spins in the spin-up state is larger than those in the spin-down state (7). It is straightforward to extrapolate from Fig. 2.1 that this will result in a non-zero M_z and $M_{xy} = 0$.

RF EXCITATION

The net/bulk magnetization ($\vec{M}$) that is generated in the presence of an external magnetic field has a severe limitation – in practice, it cannot be measured. Measuring M_z is a challenge as it is oriented along B_0 and is at-least 3 orders of magnitude smaller than B_0. Fortunately, the transverse component (M_{xy}) can be measured reliably and accurately, via electromagnetic induction, using appropriate receiver coil set-ups (7). Radio frequency (RF) excitation is the technique used to tip M_z into the transverse plane for measurement.

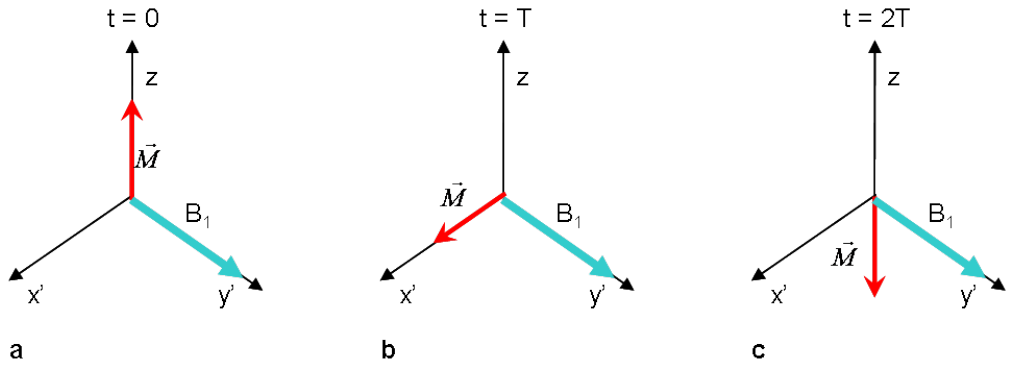

Figure 2.2: The position of M_z at different instants of time under the influence of an infinite-duration sinusoidal B_1 with $|\Omega| = \omega_0$.

Consider a sinusoidal magnetic field (B_1) of infinite duration. From basic Fourier

transform theory, the oscillations are confined to two components of equal magnitude but at frequencies $+\Omega$ and $-\Omega$, respectively. Choosing $|\Omega| = \omega_0$, the component of B_1 at $+\Omega$ is always in-phase with μ_{xy} while the other component at $+\Omega$ is always out-of-phase. The out-of-phase component can be ignored as it has no net effect. The effect of the in-phase component is best studied in a reference frame with orientation similar to the laboratory reference frame but with its transverse plane revolving in-sync with μ_{xy} (rotating reference frame). In this reference frame, the spins have a net magnetic moment (M_z) and an angular momentum with the in-phase component of B_1 acting as a constant external magnetic field. Hence, M_z precesses around B_1. This is depicted graphically in Fig. 2.2. The motion of $\vec{M}$ under the influence of B_1 is called a nutation and the frequency of precession nutational frequency (ω_n). The requirement $|\Omega| = \omega_0$ is known as the resonance condition and usually results in a Ω value in the radio frequency range giving this technique its name.

Slice Selection

Figure 2.2c strongly suggests that a B_1 of infinite length is not desirable if the tip of M_z is to be restricted to the transverse plane. Practical considerations also necessitate a RF waveform of limited duration (a RF pulse). Without proper care, using a RF pulse limits another important requirement of MR imaging – slice selection. MR imaging generally requires exciting spins in a particular slice of interest in the

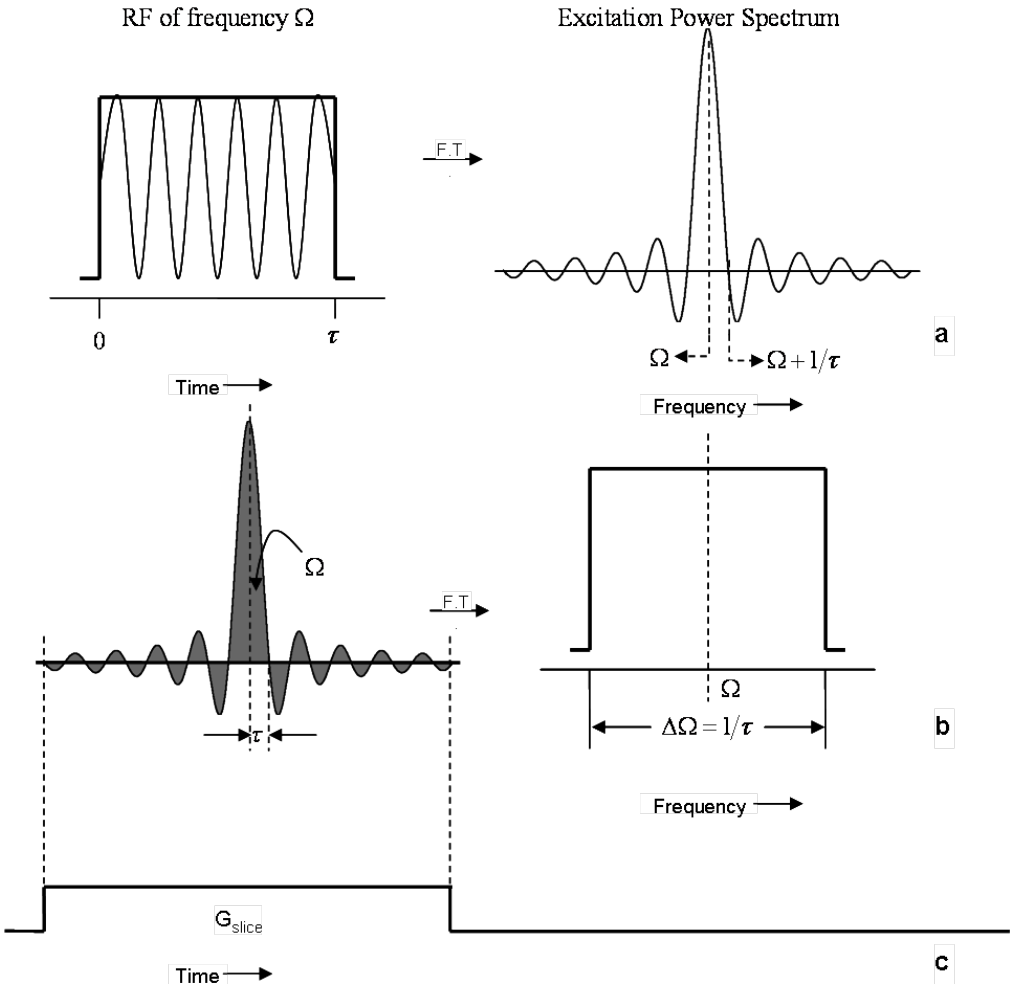

Figure 2.3: The wave shape and the corresponding excitation profile of a hard pulse (a) and SINC pulse (b) and the slice select gradient, G_{slice} (c) that accompanies the SINC pulse for proper slice selection.

object being imaged; shaped RF pulses are used for this purpose.

A sinusoidal B_1 of limited duration (hard pulse) does not deposit equal energy at all frequency components (Fig. 2.3a). This causes the spins to tip at different levels. The frequency components also extend infinitely around Ω preventing slice selection in the strict sense. Using a RF pulse with a SINC envelope, as shown

in Fig. 2.3b, deposits energy uniformly at all component frequencies which are limited around Ω. The range of component frequencies implies that the resonance condition is satisfied in a spatially dependent manner. This is exploited by inducing a spatially varying magnetic field (the magnetic field gradient G_{slice}) along the slice select direction (Fig. 2.3c) to achieve true slice selection. The description presented here is essentially for the ideal case, a more thorough treatment (8) is necessary for generating practical design equations.

Spatial Encoding

The measured signal in a NMR experiment is a net/bulk magnetization (the vector sum of the individual magnetic moments), precluding any knowledge regarding the spatial variation of the individual magnetic moments. Reliable spatial information is paramount for imaging applications. Fortuitously, the precession of the spins can be used to encode spatial information. Fourier encoding, due to its flexibility – easy extension to all 3 dimensions of space and ability to exploit the Fast Fourier Transform (FFT) construct, is the predominant spatial encoding approach.

Fourier encoding is best understood by considering the 1-D case. Extension to two and three dimensions is straight forward. Consider a horizontal 1-D ensemble of spins. The net magnetization signal (assuming appropriate excitation and slice selection) at a particular instant of time t is :

$$\sum_{\forall x} M(x)\, e^{-i\omega_0 t}. \qquad [2.8]$$

This equation follows directly from Eq. 2.5, here x is the spatial location. The time dependence of M has been ignored as it has little bearing on spatial encoding and effects, if any, can be accounted for during reconstruction. Equation 2.8 explicitly demonstrates the complete lack of spatial information in the measured signal. Now if a constant horizontal gradient (a magnetic field oriented along B_0 but varying linearly along the direction of the spin ensemble) of magnitude G is applied, the net magnetization is modified to :

$$\sum_{\forall x} M(x)\, e^{-i(\omega_0+\gamma G x)t}. \qquad [2.9]$$

The $e^{i\omega_0 t}$ term can be ignored as the received signal is always demodulated at the Larmor frequency. It is self evident that the remaining terms form the Fourier integral of $M(x)$. By continuously measuring the signal modified by an encoding gradient, the complete Fourier transform of the spin ensemble is captured. If the measurements are uniformly spaced in time, a simple FFT is sufficient to recover all the spatial information. Equation 2.9 can be used to deduce the general form of the imaging equation in 1-D with time varying gradients as :

$$\begin{aligned} S &= \sum_{\forall x} M(x)\, e^{-ixk_x} \\ k_x &= \gamma \int_0^t G_x(t)\, dt \end{aligned} \qquad [2.10]$$

Spatial information along other dimensions can also be similarly encoded using gradients played out along the respective dimensions. Spatial dimensions are usually

orthogonal to each other permitting simultaneous encoding of the required number of spatial dimensions.

RELAXATION

The RF pulse, while facilitating measurement of the net magnetization, also perturbs the thermal equilibrium of the spin system. The process by which the spins recover is called relaxation and was first described in 1946 (1). The recovery is actually achieved by two processes longitudinal or spin-lattice relaxation and transverse or spin-spin relaxation.

The two relaxation processes are independent of each other and exponential in nature. The equations describing them are known as the Bloch equations (Eq. 2.11 and Eq. 2.13). The associated time constants are dependent on the nuclear species, local chemical environment and B_0, making them distinctive characteristics of the tissues being imaged. The ability to discern tissues based on the local chemical environment of their constituent nuclei make longitudinal relaxation and transverse relaxation the basis of all contrast mechanisms in MRI.

Spin-Lattice Relaxation

The RF pulse in essence introduces vibrations to the nuclei of interest. These vibrations are dissipated by being passed on to the molecules formed by the nuclei, i.e., the lattice around the nuclei (9). If the lattice resonates at the frequency of the introduced vibrations the recovery is swift. Spin-lattice relaxation dictates the time

evolution of the longitudinal magnetization (M_z). In the rotating reference frame, the temporal variation of M_z (1) is :

$$\frac{dM_z}{dt} = -\left(\frac{M_z - M_0}{T_1}\right), \qquad [2.11]$$

giving :

$$M_z(t) = (M_z(0) - M_0)\, e^{-t/T_1} + M_0. \qquad [2.12]$$

Here M_0 is the net magnetization at thermal equilibrium and $M_z(0)$ is the longitudinal magnetization just before the application of the RF pulse.

Spin-Spin Relaxation

The individual magnetic moments result in a local magnetic field around each nucleus. These local fields can change the static external magnetic field experienced (B_{eff}) by the neighboring nuclei. Variations in B_{eff} results in de-phasing of the individual magnetic moments in the transverse plane diminishing the net transverse magnetization (9). The more stable and larger the local magnetic fields the more rapid the de-phasing and consequently faster decay of the net transverse magnetization (M_{xy}). Thus, the magnitude of M_{xy} is controlled by the spin-spin relaxation. In the rotating reference frame, the time evolution of M_{xy} can be expressed (1) as :

$$\frac{dM_{xy}}{dt} = -\left(\frac{M_{xy}}{T_2}\right) \qquad [2.13]$$

giving :

$$M_{xy}(t) = M_{xy}(0)\, e^{-t/T_2}. \qquad [2.14]$$

Here, $M_{xy}(0)$ is the transverse magnetization just after the application of the RF pulse. For a tip angle α, $M_{xy}(0) = M_z(0)\sin\alpha$.

BASICS OF MR CONTRAST

Contrast in an MR image refers to the ability to discern between tissues based on the local chemical environments of the constituent spins. MRI has such a large number of contrast mechanisms that even a brief description of the major contrast mechanisms (8) is beyond the scope of this report. The discussion here is limited to the two most basic contrast mechanisms: T_1 and T_2 weighted imaging. It is also assumed that the primary excitation pulse is a $\pi/2$ pulse (an RF pulse inducing a flip angle of $\pi/2$ is referred to as a $\pi/2$ pulse).

The concept of an echo is central to contrast in MRI. An echo is a mechanism to synchronize the individual transverse magnetic moments after a time period (T_e) following the application of the primary RF pulse. To retain focus on image contrast, echo mechanisms are described briefly here. The two predominant echo mechanisms are the spin-echo and gradient-echo. Spin-echoes are achieved by using a π pulse to flip the individual transverse magnetic moments essentially reversing the direction of precession so they will be in-sync after a period of time (7). The gradient-echo achieves the same by using the spatial encoding gradients to re-phase the individual transverse magnetic moments (7). Another vital parameter controlling MR contrast is the time to repeat (T_r) – the primary excitation pulse has

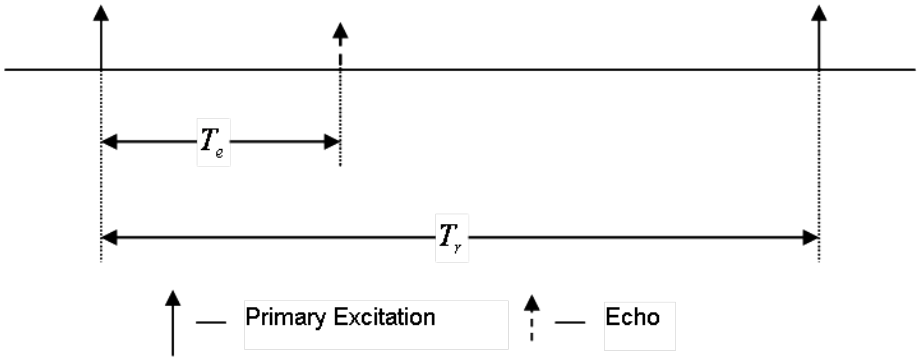

Figure 2.4: The position in time of the primary excitation pulse and the echo from an arbitrary echo mechanism.

to be repeatedly applied as generally the complete dataset cannot be acquired with just one excitation. The relationship in time between T_e and T_r for an arbitrary echo mechanism is illustrated in Fig. 2.4.

The contrast of the image is mostly influenced by the value of $M_{xy}(T_e)$. From Eq. 2.12 :

$$M_{xy}(T_e) = M_z(0)\sin\alpha e^{-T_e/T_2}. \qquad [2.15]$$

A short T_e ($T_e \ll T_2$) results in $M_{xy}(T_e) \propto M_z(0)$, i.e., the signal depends on T_r as $M_z(0)$ is the amount of longitudinal magnetization that has recovered from the last excitation. Now, choosing a short T_r ($T_r \approx 0.5\,T_1$) will generate a T_1 weighted image (the contrast is determined largely by the T_1 value of the tissue). A long T_r ($T_r \approx T_1$) permits an almost full recovery of the longitudinal magnetization, i.e., $M_z(0)$ is a constant, resulting in $M_{xy}(T_e) \propto e^{-T_e/T_2}$. Now, choosing a long T_e ($T_e \approx T_2$) will generate a T_2 weighted image.

Note that though the T_1 and the T_2 values vary with tissues; generally, for se-

quence design, the T_1 and the T_2 values for the target tissue are used.

K-SPACE TRAJECTORIES

K-space is the Fourier domain in which MR data is acquired. K-space trajectory refers to the path along which data is acquired. Time varying gradient sets allow many different options - popular trajectories are traditional raster or cartesian scan (Fig. 2.5a), projection acquisition (Fig. 2.5b) and spiral scans (Fig. 2.5c). The orientation of the data acquisition path is called the readout direction and each path is called a readout. In Fig. 2.5, the readout direction for the cartesian scan is along the horizontal and is the same for all readouts, the projection acquisition has a different readout direction for each readout, and the readout direction of the spiral scan varies with time for a readout but the variation is the same across all readouts. The readout direction is also called the frequency-encode direction and the direction perpendicular to the readout direction the phase-encode direction.

K-space trajectories are, in essence, frameworks for sampling k-space; hence, trajectory design has to comply with the Nyquist criterion and spatial resolution requirements. The Nyquist criterion for non-cartesian trajectories is generally interpreted to mean any location in k-space is within a traditional Nyquist distance from some acquired data location (7, 8, 10). Assuming an isotropic field-of-view of $F\ cm$ and resolution of $R\,cm$, for the cartesian scan (Fig. 2.5a), this means the distance between horizontal lines is $1/F cycles\ cm^{-1}$, for the projection acquisition

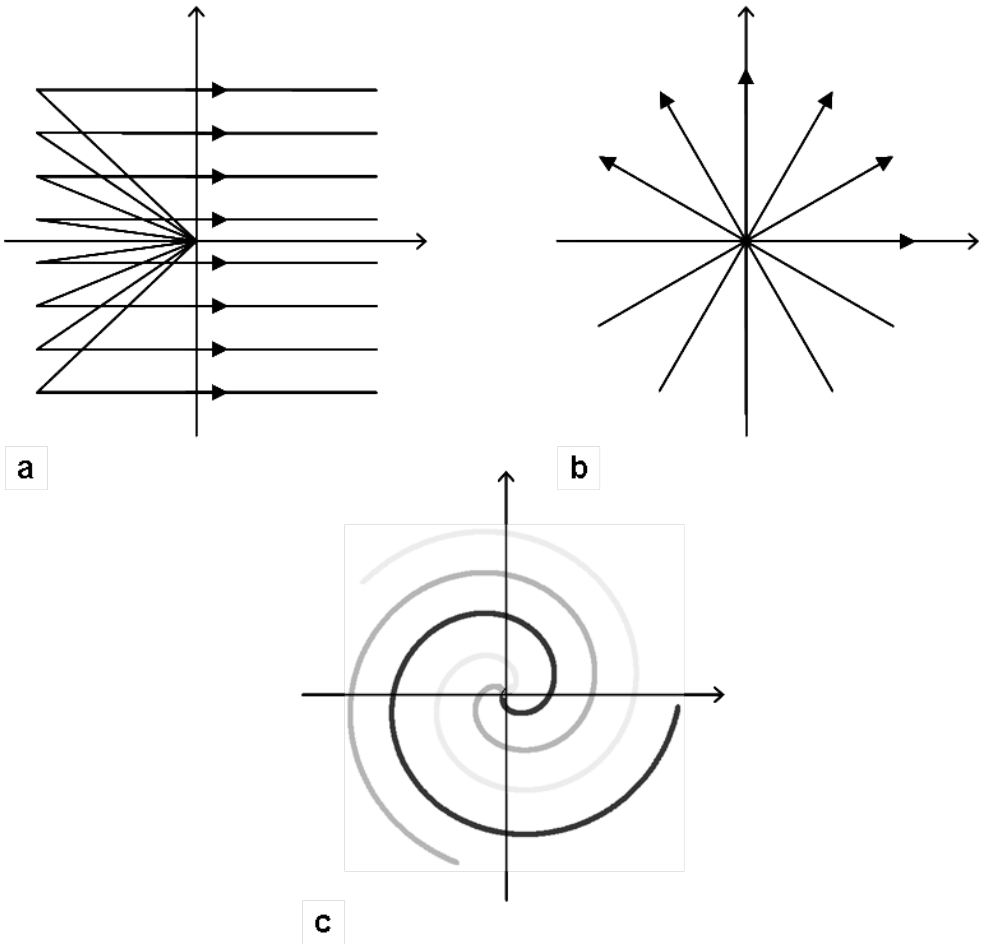

Figure 2.5: Popular 2-D k-space trajectories: traditional cartesian grid(a), projection acquisition (b), and spiral scan(c).

(Fig. 2.5b), the arc length between two spokes at their edges is $1/Fcycles\ cm^{-1}$, and for the spiral scan (Fig. 2.5c), the maximum distance between any two consecutive interval is $1/Fcycles\ cm^{-1}$. Spatial resolution is ensured by covering at-least a circle of radius $0.5/R\,cycles\,cm^{-1}$ in k-space. Trajectory design also has to account for limits on the maximum available gradient and slew $(d(Gradient)/dt)$ (8). The limits are mainly due to hardware and safety concerns.

FURTHER READING

This chapter introduced the basics of MR image formation spins, the external static magnetic field, RF excitation, slice selection, spatial encoding, relaxation, image contrast and k-space trajectories. The description presented here is based on the classical MR model and is essentially an overview. An in-depth coverage of MR imaging fundamentals, in a form that will appeal to an electrical engineer, is given by Liang *et. al.* (7). Nishimura (10) is another popular source for the first principles of MR imaging. Bernstein *et. al.* (8) is the standard source for advanced MRI topics.

Chapter 3

ELLIPTICAL FIELD-OF-VIEW PROPELLER IMAGING

Approaches to accelerated imaging are largely based on either under-sampling or fast trajectories like echo planar imaging (EPI), spiral imaging and turbo PROPELLER. Under-sampling approaches like parallel imaging strive to mitigate the effects of violating the Nyquist criterion (increased spacing between sample locations) during reconstruction and generally are computationally intensive. Scan time for anisotropic field-of-views (aFOVs) can also be reduced by tailoring the trajectory to the FOV: the Nyquist criterion for aFOVs varies with the azimuth, permitting the trajectory to be designed for larger spacing between sample locations along different directions. Previous studies have demonstrated algorithms for tailoring cartesian (11, 12), radial (11, 13, 14) and spiral (15) trajectories.

The essence of a tailored trajectory approach is specifying and complying with a local Nyquist criterion. The advantage of conforming to the Nyquist criterion is minimal computational overhead, but the savings in scan time depends on the degree to which the FOV is anisotropic and is usually modest. Tailored PROPELLER can potentially be beneficial in spine imaging (FOV is anisotropic to a high degree) and diffusion weighted brain-imaging (the modest savings in scan time accumulated over a large number of acquisitions results in substantial overall savings). This work assumes elliptical FOV (eFOV) because, in practice, most aFOVs are

elongated regions which can be approximated by an ellipse.

The blades of a PROPELLER scan are usually acquired by systematically rotating the gradient coordinate system of the scanner. For an eFOV, the FOV varies along both the phase-encode direction (PED) and frequency-encode direction (FED) at each angular position (Fig. 3.1c). It is straightforward to vary the phase-encode step size to match the FOV along the PED for each blade. The practical implementation is further simplified if all blades are required to have the same number of phase-encodes. The step size along the FED can also be set to support the largest required FOV (the major axis of the eFOV) as this has negligible effect on scan time. Supporting a variable FOV in the PED with a fixed number of phase-encodes and the FED step size supporting the largest FOV, has an unique effect on the PROPELLER trajectory: blade width varies with angular position forming an elliptical central region in k-space that is sampled by all blades (the shaded region in Fig. 3.1d; hereafter referred to as the ellipse-of-overlap). In the case of an isotropic field-of-view (iFOV), this region is circular (the shaded region in Fig. 3.1b; hereafter referred to as the circle-of-overlap). By a proper choice of the angular sampling scheme, the presence of wider blades can be leveraged to critically sample (the maximum distance between any two sample locations is the Nyquist distance) k-space with fewer blades resulting in reduced scan time; the larger is the variation in blade width, the greater are the savings in scan time.

Radial trajectories need a non-uniform angular sampling scheme to take ad-

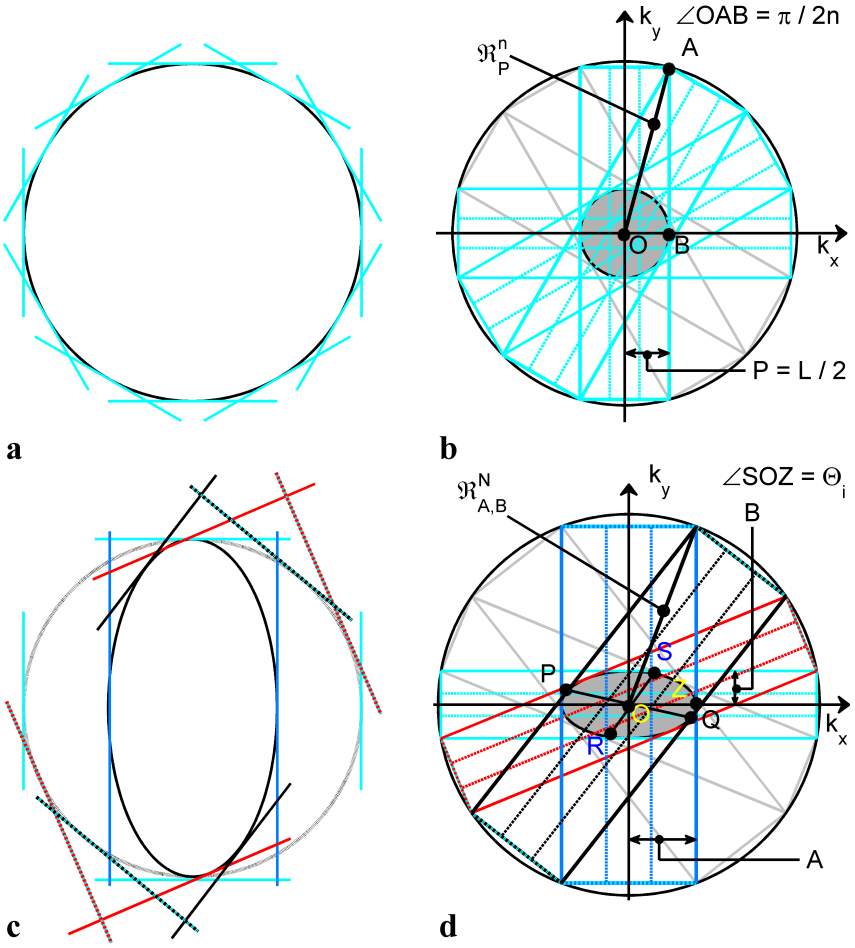

Figure 3.1: Image space orientation and the corresponding blade configuration in k-space for isotropic FOV (a and b) and elliptical FOV (c and d). The edges of the blade have been color coded to indicate the supported FOV. The long and short edges for eFOV blades (with the exception of the first blade) are colored differently to illustrate that they support separate FOVs along the PED and FED.

vantage of an aFOV (11, 13, 14). The PROPELLER trajectory is also radial in nature, suggesting a similar approach to tailoring it for an eFOV. The algorithm presented here utilizes the PROPELLER geometry to generate a non-iterative empirical closed-form solution. It further specifies the minimum number of blades

necessary to critically-sample k-space, helping retain a scan prescription procedure similar to standard PROPELLER. The results are also consistent with those from an iterative approach (16).

PROPELLER TRAJECTORY DESIGN

Mathematical formulation is simple if the major axis of the eFOV is assumed to be aligned with the initial PED of the scanner. In practice, this is not a restriction as the initial FED orientation can be set by the operator. This work assumes left/right as the initial FED orientation leading to a horizontal first blade. Further, the blade along the major axis of the eFOV is the widest and that along the minor axis of the eFOV is the narrowest indicating that the major axis of the ellipse-of-overlap is aligned with the minor axis of the eFOV (Fig. 3.1c and Fig. 3.1d).

A review of iFOV design will serve to introduce notation, PROPELLER geometry and trajectory design. The iFOV PROPELLER trajectory design specifies the number of blades from operator requirements; the blade angles are then generated using the specified number of blades. With fixed operator requirements, the number of blades is a function of the central region of overlap in k-space. This relationship is dictated by the PROPELLER geometry.

iFOV PROPELLER

The iFOV PROPELLER trajectory has a distinct geometry : given the radius of the circle-of-overlap (P) and the number of blades (n), there is an unique circle – the

critical circle – on which the vertices of consecutive blades coincide (Fig. 3.1a). In terms of sampling, the critical circle is the biggest circle in k-space which is critically-sampled by n blades each of width $2P$. From Fig. 3.1a, the radius of the critical circle ($\Re_P^n$) is given by :

$$\Re_P^n = \frac{P}{\sin\left(\frac{\pi}{2n}\right)}. \qquad [3.1]$$

Assuming large n (i.e. $n \gg \pi/2$) permits the polygon formed by the blades to approximate the critical circle giving the blade length as $2\Re_P^n$.

The iFOV PROPELLER trajectory design (17) generates the minimum number of blades necessary to critically sample k-space (n_{min}) using Eq. 3.1 with P and $\Re_P^n$ specified by operator requirements. In an actual scan, the blade width is equal to the number of phase encodes per blade (L) giving $P = L/2$ and $\Re_P^n = M_{eff}/2$, where $M_{eff} = FOV/resolution$. Using the small angle approximation for the sine term (as $n \gg \pi/2$) in Eq. 3.1 gives

$$n_{\min} = \left(\pi M_{eff}\right)/2L. \qquad [3.2]$$

The over-sampling factor (*nex*) is accounted for by extending Eq. 3.2 as

$$n = nex\left(\pi M_{eff}/2L\right). \qquad [3.3]$$

Once the number of blades is determined, the blade angles (θ_i) are generated from

$$\theta_i = (i-1)\,\theta_0, \qquad [3.4]$$

where $\theta_0 = \pi/n$.

Number of Blades for eFOV

An eFOV is characterized in image space by FOV_{short} (the minor axis of the eFOV) and FOV_{long} (the major axis of the eFOV). In k-space, it is characterized by N, N_{min}, Θ_i (the equivalents of n, n_{min} and θ_i, respectively), the semi-major (A) and semi-minor (B) axes of the ellipse-of-overlap (Fig. 3.1b), and the ellipse ratio (r) defined as

$$r = B/A = FOV_{short}/FOV_{long} \qquad [3.5]$$

Here FOV_{short} and FOV_{long} refer to the small and large dimension of the $eFOV$ (in image space) respectively. The proposed angular sampling scheme is designed to mimic the geometry of the standard PROPELLER trajectory. This ensures that the concept of a critical circle is preserved for an eFOV. A closed form expression for the radius of the critical circle for an eFOV ($\Re^N_{A,B}$) is vital for a design solution similar to that for iFOV. Deriving an equation for $\Re^N_{A,B}$ is mathematically intractable due to the complex equations that are involved. Instead, it is relatively simple to show empirically (page 31) that

$$\Re^N_{A,B} \approx \left(2\Re^N_{\alpha} + \Re^N_{\beta}\right)\Big/3. \qquad [3.6]$$

Here $\Re^N_{\alpha}$ is the radius of the critical circle for an iFOV PROPELLER trajectory with N blades and a circle-of-overlap whose area is equal to that of the ellipse-of-

overlap. Thus α, the radius of the circle-of-overlap, is given by

$$\alpha = \sqrt{E_a/\pi}, \qquad [3.7]$$

where E_a = Ellipse Area = πAB. Similarly, $\Re_\beta^N$ is the radius of the critical circle for an iFOV PROPELLER trajectory with N blades and a circle-of-overlap whose perimeter is equal to that of the ellipse-of-overlap. Hence β, the radius of the circle-of-overlap, is given by

$$\beta = E_p/2\pi, \qquad [3.8]$$

where E_p = Ellipse Perimeter = $\pi(A+B)\left(1+\frac{3h}{10+\sqrt{4-3h}}\right)$ and $h = \left(\frac{A-B}{A+B}\right)^2$. The expression for the ellipse perimeter is an approximation proposed by Ramanujan (18).

Analogous to the iFOV design process, operator requirements give $B = L/2$, $A = B/r$ and $\Re_{A,B}^N = M_{eff}/2$. Here, $M_{eff} = FOV_{long}/resolution$ (eFOV scans have isotropic resolution as the blades have equal length). With A, B and $\Re_{A,B}^N$ specified and still assuming $N \gg \pi/2$, N_{min} can be generated from Eq. 3.6 and Eq. 3.1 as

$$N_{\min} = \frac{3\pi M_{eff}}{4(2\alpha+\beta)} \qquad [3.9]$$

and accounting for *nex* gives

$$N = \frac{nex\ 3\pi M_{eff}}{4(2\alpha+\beta)}. \qquad [3.10]$$

Blade Angles for eFOV

It is instructive to compare Θ_i with θ_i for identical L, M_{eff} and $N = n$. From a simultaneous plot of Θ_i and θ_i (Fig. 3.2a), it is evident that Θ_i follow θ_i with sinusoidal

deviations. This is yet another effect of blades with varying width – beginning with the horizontal blade, the blades get wider (with respect to the horizontal blade) and need to rotate less to maintain the standard PROPELLER geometry; but from the vertical blade onwards, the blades get thinner (with respect to the vertical blade) and need to rotate more to maintain the standard PROPELLER geometry. The difference $\Theta_i - \theta_i$ (r_1 in Fig. 3.2b) suggests that $\Theta_i \approx \theta_i + k_1 \sin 2\theta_i$ (k_1 is a weighting factor to be determined) and $\Theta_i - [\theta_i + k_1 \sin 2\theta_i]$ (r_2 in Fig. 3.2b) hints at a more refined estimate :

$$\widehat{\Theta}_i = \theta_i + k_1 \sin 2\theta_i + k_2 \sin 4\theta_i. \qquad [3.11]$$

Again k_2 is a weighting factor to be determined. The order of the residual $\Theta_i - \widehat{\Theta}_i$ (r_3 in Fig. 3.2b) is tolerable in practice (19).

The only pre-determined values of Θ_i are 0 and $\pi/2$ (assuming even number of blades); unfortunately, they are not helpful in solving for k_1 and k_2, necessitating an empirical approach. The structure of Eq. 3.11 suggests that the two weighting factors are functions of both r and N. Blade angles Θ_i can be determined at all practical values of r and N using the recursive approach detailed in the following section. Curve fitting Eq. 3.11 to these predetermined values of Θ_i will determine k_1 and k_2. From Figs. 3.2c-d, it is evident that N has negligible effect on the values of k_1 and k_2. The numerical values of k_1 and k_2 are then fit to a bi-exponential

giving

$$k_1 = 0.4391e^{0.4515r} - 0.4607e^{-4.985r} - 0.6803$$
$$k_2 = 0.09514e^{-5.048r} + 0.09781e^{-23.06r}. \quad [3.12]$$

As described in the following section, Θ_i can be generated recursively based on the knowledge of $\Re^N_{A,B}$. Nonetheless, a closed form solution is preferred as it enhances the ease of implementation.

Generating Θ_i Recursively

Given A, B, N, $\Re^N_{A,B}$ with blade length set to $2\Re^N_{A,B}$, consider the kth blade (b_k). The long edges of a blade are always tangential to the ellipse-of-overlap (Fig. 3.1b). From co-ordinate geometry, each vertex of b_k has only one unique pair of tangents to the ellipse-of-overlap and these tangents are not parallel to each other. Given that the blade length is $2\Re^N_{A,B}$, the critical circle by definition forces b_k to share each of its vertices with either b_{k-1} or b_{k+1}. This implies that of the two tangents to the ellipse-of-overlap from any vertex of b_k, one is a long edge of either b_{k-1} or b_{k+1} as the other is a long edge of b_k itself. Therefore if Θ_k is known, Θ_{k+1} can be deduced using an appropriate vertex of b_k as the guide/seed point. The angle between the pair of tangents (Φ) from the seed point to the ellipse-of-overlap can be computed by comparing the equation for the tangent pair to the equation for a line pair. It is evident that $\Theta_{k+1} = \Theta_k + \Phi$. The tangent that is a long edge of b_{k+1} (specified by the current seed point and Θ_{k+1}) is a cord of the critical circle; thus, the next seed point is given by the other end of this cord. The angular position of

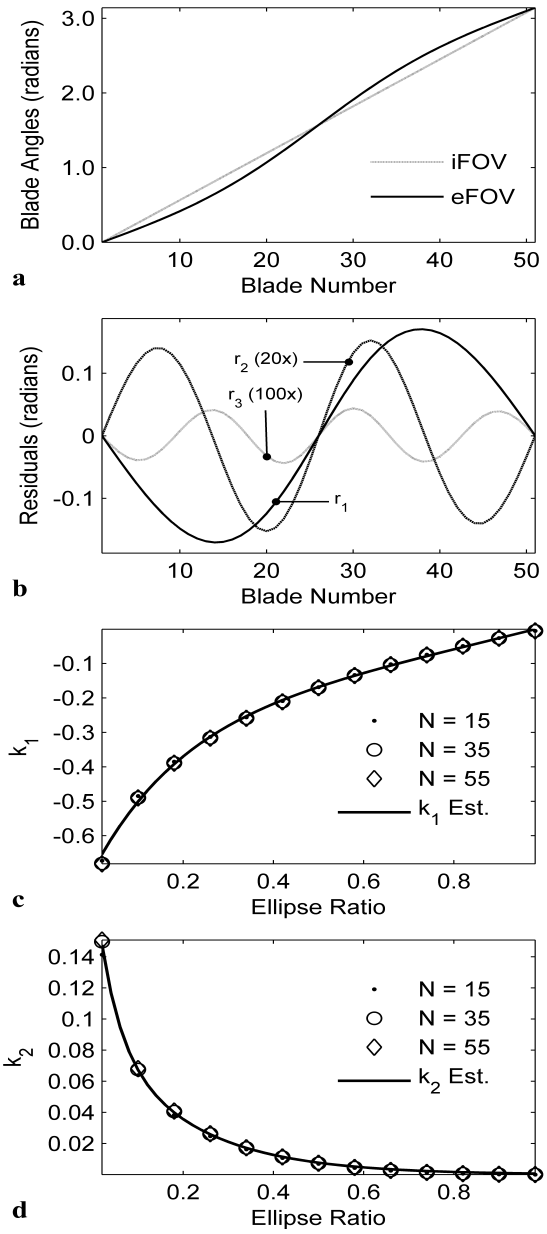

Figure 3.2: Blade angles from a typical eFOV scan in comparison to a similar iFOV scan (a). The residuals when Θ_i are approximated by θ_i and a series of sine terms (b). Here $r_1 = \Theta_i - \theta_i$, $r_2 = \Theta_i - [\theta_i + k_1 sin(2\theta_i)]$ and $r_3 = \Theta_i - [\theta_i + k_1 sin(2\theta_i) + k_2 sin(4\theta_i)]$. The computed and estimated (from Eq. 3.12) values of k_1 (c) and k_2 (d) as a function of r (ellipse ratio) with different N (number of blades). It is evident that the effect of N on k_1 and k_2 is minimal.

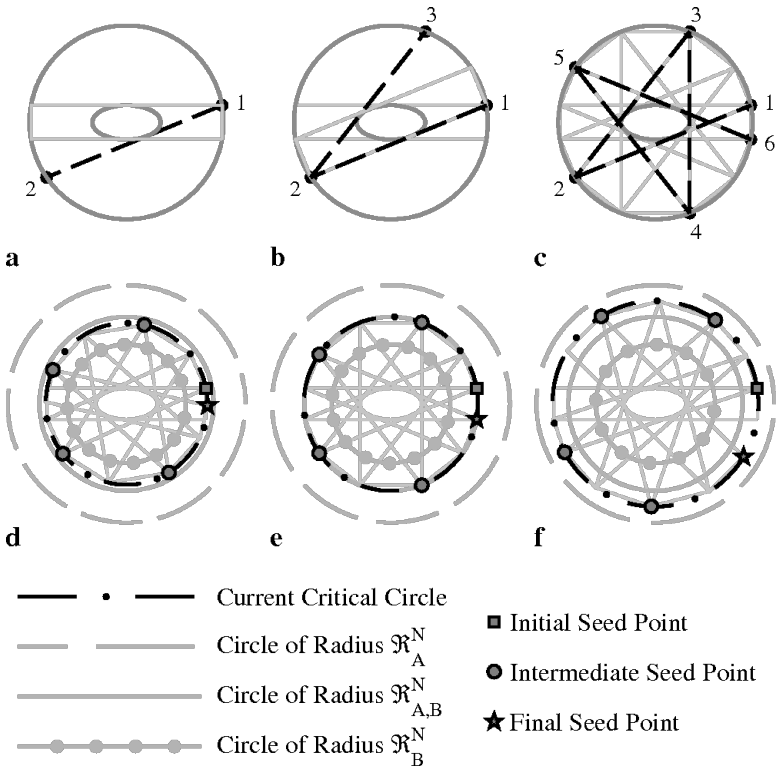

Figure 3.3: Blade angles are generated recursively (a-c) based on a seed point (labeled consecutively) provided by the previous blade. The dashed line indicates how the next seed point is generated by the current seed point. The iterative procedure to determine $\Re^N_{A,B}$ (d-f) follows from recursively generating the blade angles. Constraining the estimates to be between $\Re^N_B$ and $\Re^N_A$ helps in rapid convergence to the final solution (e). As indicated by the intermediate estimates (d and f), the vertical position of the final seed point is a good indicator of estimation error.

the initial blade is always known, making the initiation of this recursive algorithm trivial. Due to the assumed orientation of the eFOV, in this work, the initial blade is horizontal ($\Theta_1 = 0$). Figures 3.3a-c graphically describe this procedure beginning with the initial blade.

Empirically Determining $\Re^N_{A,B}$

The recursive approach outlined above has a valuable feature: the actual final seed point can be pre-determined (Fig. 3.3c). If an estimate of $\Re^N_{A,B}$ is used in the recursive algorithm, the vertical position of the achieved final seed point is a good indicator of whether the estimate is greater or lesser than the actual value. This information can be used to iteratively improve the estimates via bisection till the required accuracy is attained (Figs. 3.3d-f). The initial range of $\Re^N_B < \Re^N_{A,B} < \Re^N_A$ was sufficient for a quick convergence.

Equation 3.6 can be derived empirically using this procedure. $\Re^N_{A,B}$ is estimated at all practical values of r ($0 < r \leq 1$ in steps of 0.05) and N ($10 \leq N \leq 200$ in steps of 5). The ratio $\kappa = \left(\Re^N_{A,B} - \Re^N_\alpha\right) \Big/ \left(\Re^N_\beta - \Re^N_{A,B}\right)$ can then be computed at each value of r and N. The computed values reveal that $\kappa \approx 0.5$, a constant immune to variations in r and N, validating Eq. 3.6.

eFOV In Practice

In practice, N is determined by Eq. 3.10 then Θ_i by Eq. 3.11 and Eq. 3.12. The blade width and the associated phase-encode step size ($StepSize_{PE} = BladeWidth/L$) for each blade can then be inferred using co-ordinate geometry. Consider the line segments PQ and SR in Fig. 3.1b, it is evident that they are conjugate diameters of the ellipse-of-overlap. Given the blade angle and the dimensions of the ellipse-of-overlap, the point P can be determined by the equation for the gradients of the

conjugate diameters and the equation for the ellipse-of-overlap. Point P, with the blade angle, specifies the equation for the corresponding long edge of the blade. The blade width is twice the perpendicular distance of the origin from this long edge.

A water-phantom experiment is ideal to verify the attained FOV and SNR of the new trajectory. In-vivo experiments further validate the trajectory. A scan with the major axis of the eFOV not aligned with the initial PED to demonstrate the possible aliasing errors, was included in both experiments. All experiments were conducted on a 3T GE HDX scanner using a modified PROPELLER FSE sequence. All scans were axial, 5 mm thick single-slice acquisitions.

The eFOV and iFOV scans for the water-phantom experiment were prescribed with $ETL = 47$, $T_r = 2400\,ms$, $T_e = 166\,ms$, $resolution = 0.98\,mm$ and $nex = 1$. Here ETL refers to the echo train length and specifies the blade width. The iFOV trajectory was designed for a $FOV = 26\,cm$, while the eFOV trajectory was designed for an $FOV_{short} = 13\,cm$ and $FOV_{short} = 26\,cm$. The in-vivo experiments were prescribed with $ETL = 47$, $T_r = 4000\,ms$, $T_e = 87.6\,ms$, $resolution = 0.75\,mm$ and $nex = 1$. The iFOV trajectory now supported a $FOV = 24\,cm$, while the eFOV trajectory supported a $FOV_{short} = 18\,cm$ and $FOV_{short} = 24\,cm$.

The eFOV trajectory is designed to yield either a critically sampled or over-sampled k-space allowing standard gridding reconstruction (20) with sampling density correction (21). Hence, the eFOV PROPELLER reconstruction differs from

standard PROPELLER reconstruction in only the k-space locations used to grid the acquired data. Requiring the major axis of the eFOV to be aligned with the initial PED of the scanner, while simplifying the mathematical formulation, also ensures that the first blade has equal phase encode and frequency encode step sizes. This is sufficient to specify the semi-major (A) and semi-minor (B) axes of the ellipse-of-overlap and the ellipse ratio (r). Equation 3.11 and Eq. 3.12 can now be used to determine the blade angles. The phase-encode step size for each blade can then be computed as described above.

The achieved FOV is best established by the point spread function (PSF) of the designed trajectory. The full PSF (2FOV wide) was computed by gridding, with sampling density correction, a dataset of all ones to a grid of spacing $0.5/FOV_{long}$ and transforming to image space. The generated PSFs were then raised to a power of 0.35 to aid in better visualization of the achieved FOVs.

With other scan parameters being fixed, a reduced scan time implies reduced SNR. The SNR ratio of two comparable PROPELLER scans with different number of blades is expected to be proportional to the ratio of the number of blades as the achieved SNR is proportional to the square root of the total ADC time, and the total ADC time of a PROPELLER scan is proportional to the number of blades in the scan. The SNR values for the water phantom experiments were determined using the single-image approach (22), while the SNR values for the in-vivo experiments were computed via the dual-image approach (22).

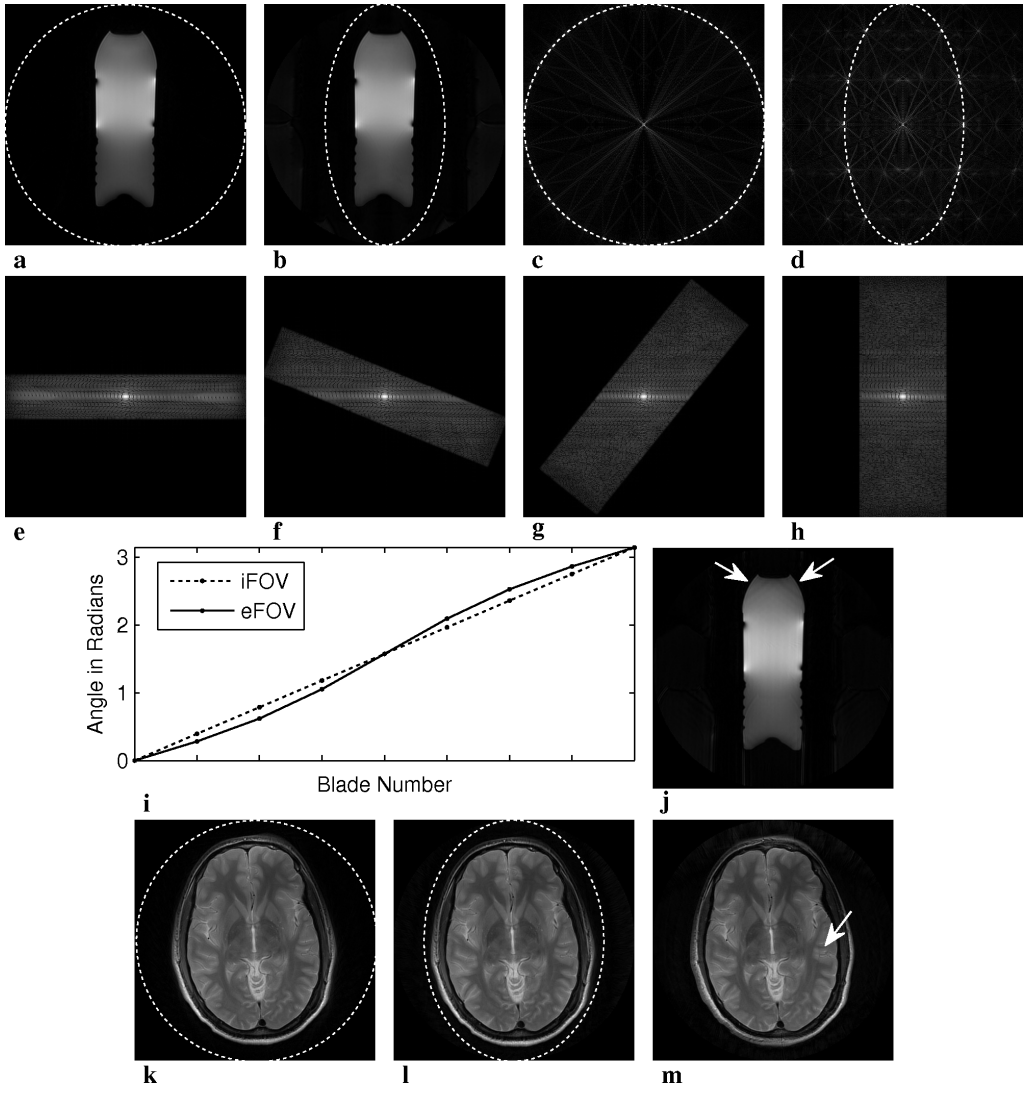

Figure 3.4: Water phantom image eFOV (b) in contrast to iFOV (a) with the corresponding PSFs (c-d). Individual blades showing variation in blade width (e-h) and the generated angles (i). Volunteer image eFOV (l) and iFOV (k). The possible aliasing artifacts when the major axis of the eFOV is not aligned with the initial PED for the water phantom (j) and the volunteer (m).

RESULTS

The water-phantom experiments produced an eFOV scan with $N = N_{min} = 6$ ($M_{eff} = 265$; Scan Time $= 32\,s$) and an iFOV scan with $n = n_{min} = 9$ ($M_{eff} = 265$; Scan Time $= 39\,s$). The in-vivo experiment yielded an eFOV scan with $N = N_{min} = 21$ ($M_{eff} = 320$; Scan Time $= 104\,s$) and an iFOV scan with $n = n_{min} = 25$ ($M_{eff} = 320$; Scan Time $= 120\,s$).

The final water-phantom images from iFOV (Fig. 3.4a) and eFOV (Fig. 3.4b) scans are visually similar. The achieved SNR values are in agreement with the expected values ($SNR_{eFOV}/SNR_{iFOV} = 75.5/91.7 = 0.823 \approx 0.816 = \sqrt{6/9} = \sqrt{N_{\min}/n_{\min}}$).The varying blade width of the eFOV scan is clearly visible in Figs. 3.4e-h, and the generated angles (Fig. 3.4i) follow the pattern described before. The aliasing errors when the major axis of the eFOV is not aligned with the initial FED (Fig. 3.4j) are not dramatic but still visually discernible.

The corresponding full PSFs for iFOV (Fig. 3.4c) and eFOV (Fig. 3.4d) clearly exhibit the circular and elliptical FOV that the trajectories were designed for. The seemingly aggressive streaking in the PSFs is a secondary by-product of raising the PSFs to a fractional power. Since the trajectories are designed to at least critically sample k-space, the residual streaks are just as likely due to imperfections in gridding and sampling density correction as due to the trajectory itself, confounding any quantitative analysis.

The in-vivo images (iFOV in Fig. 3.4k and eFOV in Fig. 3.4l), again, are visually similar. The achieved SNR ratio concurs with the estimated ratio ($SNR_{eFOV}/SNR_{iFOV} = 62.4333/69.0736 = 0.904 \approx 0.916 = \sqrt{21/25} = \sqrt{N_{\min}/n_{\min}}$). Due to a more rounded FOV ($r = 0.75$), the aliasing errors when the major axis of the eFOV is not aligned with the initial FED (Fig. 3.4m) are more benign than those for the water phantom.

eFOV Trajectory Performance

Other angular sampling schemes can also be used for tailoring the PROPELLER trajectory to an eFOV. Consecutive blades, in a standard PROPELLER scan, advance by a constant angle, traversing arcs of constant length on the circle-of-overlap. This suggests two alternatives to the proposed non-uniform angular scheme – equi-angle (blades advance by a constant angle) and equi-arc (blades advance by traversing arcs of constant length on the ellipse-of-overlap). However, for a fixed M_{eff} and a fixed *nex*, both of these schemes require more blades to critically sample k-space than the proposed scheme (Figs. 3.5a-c). The proposed scheme offers the maximum savings in scan time (smallest N_{min}) while preserving the standard PROPELLER geometry to a large extent.

A similar geometry permits a design procedure that is similar to a standard scan, making practical application straightforward, and also gives a direct measure of reduction in scan time – N_{min}. From Eq. 3.9, N_{min} is a function of r, and Fig. 3.5d

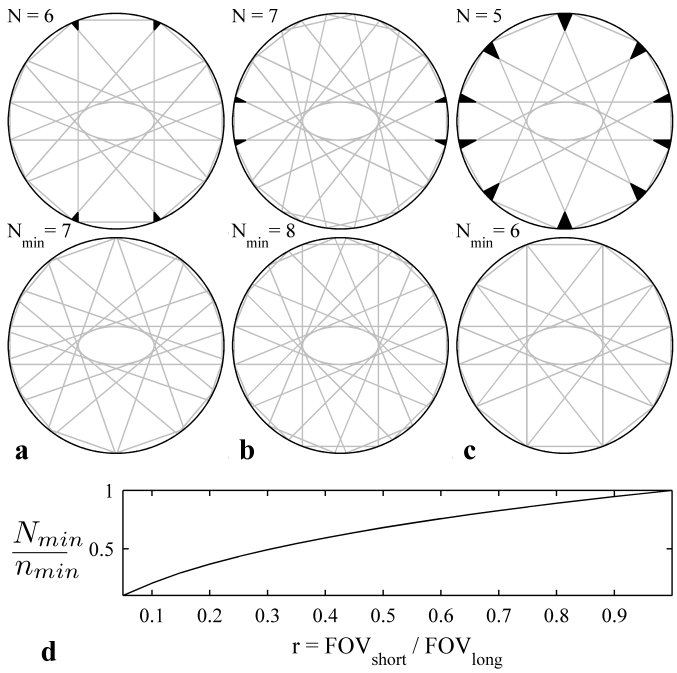

Figure 3.5: Various angular sampling schemes in comparison to each other - equi-arc (a), equi-angle (b) and proposed (c). N_{min} as a measure of potential savings in scan time (d) for $L = 47$ and $M_{eff} = 265$.

illustrates potential savings as a function of r. Greater savings are observed for more elongated FOVs. In general, the human head has $r \approx 0.7$ and, for r in this range ,N_{min} is less than n_{min} by just 20 percent. Despite the modest savings, when applied to protocols needing repeated acquisitions, the accumulated overall savings will potentially be substantial.

The proposed non-uniform angular sampling scheme is similar to the one generated by the iterative approach (16) with the added advantage of specifying N_{min}, making it possible to design a scan based on operator prescription similar to iFOV. Since the algorithm needs to be implemented on both the scanner and the recon-

struction computer, the iterative approach may also result in different angles due to differences in hardware architecture and software library used.

As the proposed trajectory maintains standard PROPELLER geometry, implementing PROPELLER motion correction just requires using updated k-space coordinates. This is further facilitated by the constant step size along the FED. This ensures that, though the proposed trajectory is designed for an eFOV, the receiver bandwidth of the scanner supports a full iFOV eliminating any blurring due to the object moving out of the eFOV. In practice, *nex* can be increased such that discarding a couple of corrupted blades will not affect the final image.

SUMMARY

This work introduces an empirical non-iterative closed-form solution for tailoring the PROPELLER trajectory to an elliptical FOV for reducing scan time. The performance has been experimentally demonstrated to be comparable to standard PROPELLER scans. The prescription and reconstruction procedures are largely similar to standard PROPELLER, making practical application straightforward. Though the possible savings are a function of the FOV dimensions, when applied to protocols requiring a large number of acquisitions, like diffusion weighted PROPELLER, even FOVs with modest reductions will potentially result in significant overall savings.

Chapter 4

MEASURING GRADIENT COUPLING FOR SPIRAL TRAJECTORIES

Gradient delays are the first-order manifestations of gradient system imperfections (8). These delays cause a timing mismatch between different gradient channels and data acquisition (Fig. 4.1), resulting in reduced image quality. The image degradation is pronounced in non-Cartesian scans like spiral imaging. Figure 4.2 illustrates the potential artifact via a simulation. The cost of mismatch is further accentuated in 3D scans like Spiral Projection Imaging (SPI).

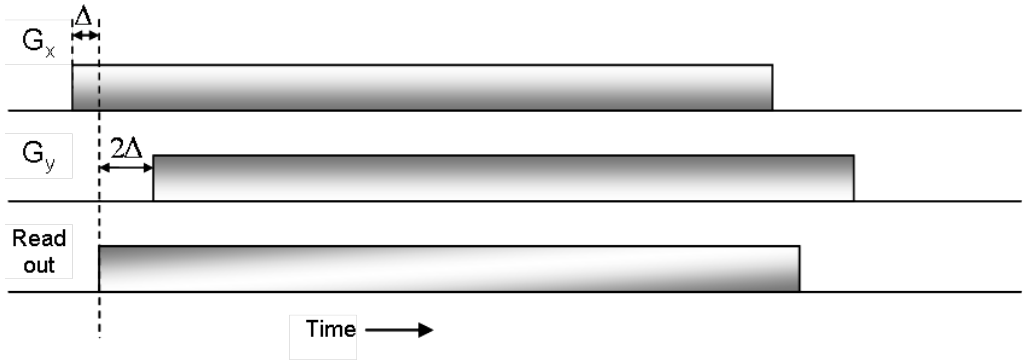

Figure 4.1: An example of timing mismatch between gradients and readout for an arbitrary axial 2D trajectory.

Current methods (23, 24, 25, 26) to measure and correct gradient imperfections are usually based on measuring delays while playing out waveforms on an individual gradient channel. However, spiral scans, particularly SPI (3D non-cartesian scan), require waveforms to be played out concurrently on two or more gradient channels, making it necessary to account for delays due to interactions between the

gradient channels, if they exist. This work presents a simple approach to measuring the changes (if any) in gradient delays due to gradient coupling while playing out spiral waveforms.

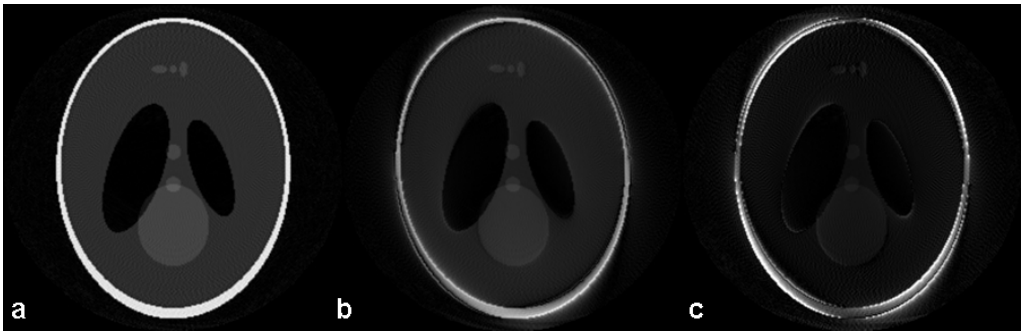

Figure 4.2: Artifact in a 2D spiral reconstruction from the timing mismatch shown in Fig. 4.1 for $\Delta = 0\mu s$ (a); $\Delta = 3\mu s$ (b); difference image to better illustrate the artifact (c). All images are windowed identically

THE MEASUREMENT ALGORITHM

While playing out a waveform on a gradient channel, a delay results in a delayed or shifted acquisition of k-space data. Traversing the k-space trajectory associated with the waveform in the opposite direction forces the collected k-space data to shift in the opposite direction. Since the amount of both shifts is the same, they can be estimated by cross-correlating the two acquired k-space sequences. A shift in the k-space sequence is a direct consequence of the gradient delay; hence, any measure of the shift is also an estimate of the delay. Interaction between two gradient channels (if any) will affect the gradient delay on both channels. The effect on any one gradient channel can be measured by concurrently playing out the ad-

ditional waveform on the other gradient channel while following the measurement procedure described above.

Traversing the k-space trajectory in the opposite direction is straight forward: the same waveform is played out, only with the sign reversed. Fig. 4.3a depicts the k-space trajectory pair that can be used to measure the effect of coupling between x and y gradient channels on the x channel for a 2D spiral sequence. A vertically uniform k-space, particularly a function of the form $M(k_x, k_y) = \delta(k_x)$ (the dark vertical line in Fig. 4.3a), will facilitate having a substantial signal near the cross-over sections of the trajectories and will minimize the difference in the k-space structure due to the divergent paths of the two segments. This can be achieved by selectively exciting a horizontal line of spins or by a line phantom. This work utilized the line phantom due to the practical simplicity of this approach. The necessity of the line phantom is evident in the zoomed-in portion of Fig. 4.3a – without the k-space structure of the phantom, the amount of overlap between the two trajectories is minimal and is not conducive for estimating shifts via correlation.

Measurements In Practice

The k-space shift was measured by correlating the magnitude data from corresponding segments of the trajectory pairs and determining the shift of the peak correlation value from its expected position. The expected position of the peak correlation had to be computed for every segment, as the trajectory design does not always ensure

a data acquisition location at the point of overlap. This measured k-space gap can then be used to estimate the time delay using the approximation that an incremental change in time is equal to an incremental change in k-space normalized by the product of the gradient strength G and the gyromagnetic ratio γ as given by:

$$\frac{dk}{dt} = \gamma G \qquad [4.1]$$

Separate delays are measured for each overlapping segment and the results averaged to yield a single time delay for the gradient channel.

The line phantom was constructed by sandwiching a thin layer ($< 1mm$ thick) of water-based gel between two plates of glass (Fig. 4.4a). Glass plates, approximately $23cm$ long and $7cm$ wide, were found to be convenient (Fig. 4.4b). The gradient

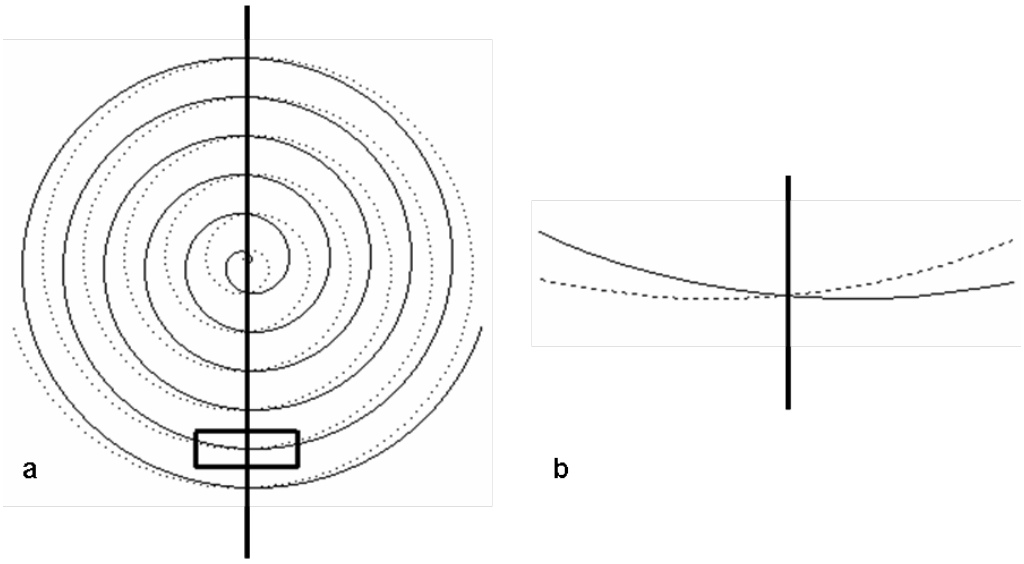

Figure 4.3: A typical k-space spiral trajectory pair to measure the effect of coupling between x and y gradient channels on the x channel for a 2D spiral sequence (a). A zoom-in of the marked portion (b) depicts the amount of overlap between the two trajectories.

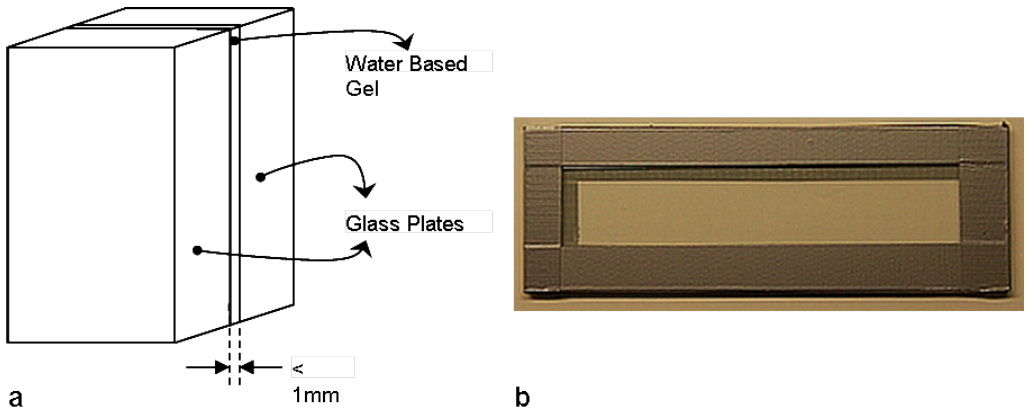

Figure 4.4: Schematic of the line phantom (a) and the actual constructed phantom (b).

delays can be measured in each of the three imaging planes. The phantom needs to be oriented appropriately for each plane (Fig. 4.5). Each of the planes gives the delays for two gradient sets x and y gradient delay from the axial (x-y) plane, y and z gradient delay from the sagittal (y-z) plane, x and z gradient delay from the coronal (x-z) plane. The multiple measurements serve to cross-validate the estimates. If the line in k-space is non-orthogonal to the orientation of the gradient channel being studied, measurements can be considerably skewed. Hence, a six-inch plastic level was used to position the phantom orthogonally to the orientation of the gradient channel being considered.

RESULTS

All experiments were conducted on a GE Signa Excite 3T scanner with a 150/40 gradient system. The constructed line phantom (Fig. 4.4b) was first tested in the orientation depicted in Fig. 4.5a with a stock Cartesian gradient-echo (SPGR) se-

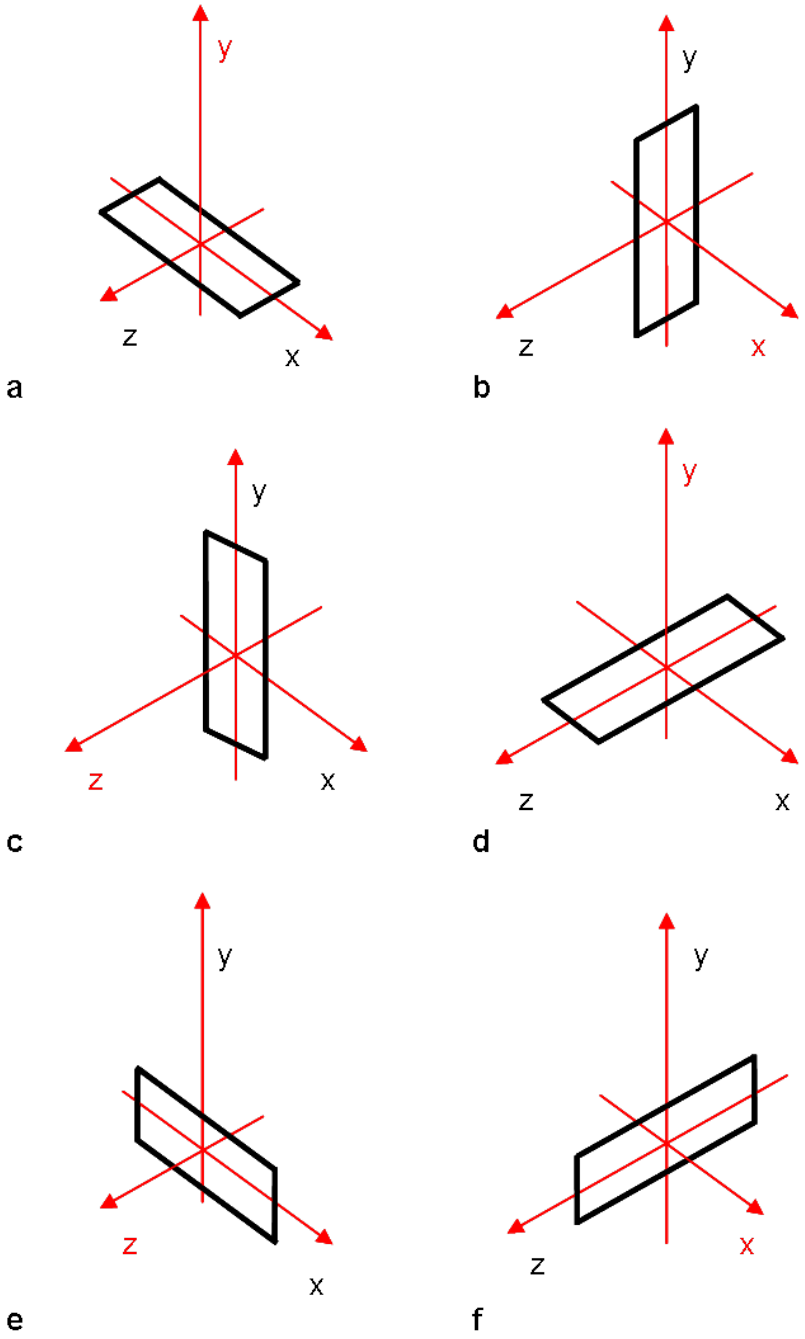

Figure 4.5: Phantom orientations for gradient delay measurement in the three imaging planes: axial plane (a,b); sagittal plane (c,d); coronal plane (e,f). In all the images, the axes labeled in the same color as the phantom (black) indicate the plane which contains the phantom. These orientations give multiple measurements of the delays: x gradient delay (a,e); y gradient delay (b,c); z gradient delay (d,f).

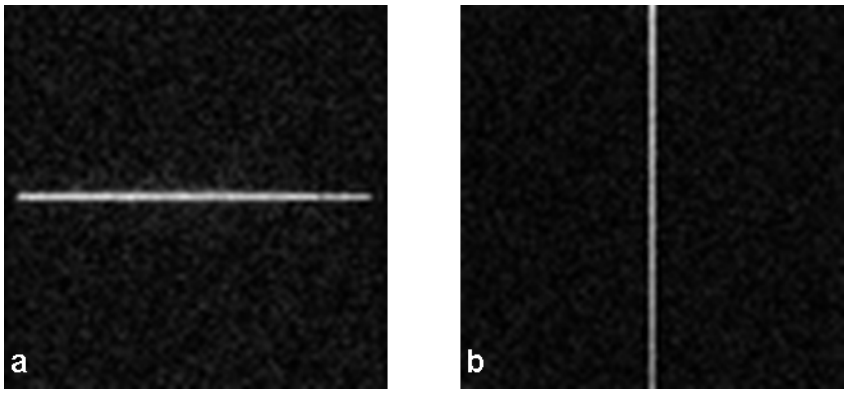

Figure 4.6: The achieved image space (a) and k-space (b) from the constructed phantom. The phantom was in the orientation depicted in Fig. 4.5a.

quence. The resulting image-space (Fig. 4.6a) and k-space data (Fig. 4.6b) are consistent with the design objectives suggesting that positioning with a plastic level is adequate.

A 2-D constant density spiral trajectory designed for a 24*cm* FOV, 1*mm* isotropic resolution and 16 spiral interleaves, was used to measure the gradient delays in the axial, sagittal and coronal planes. The estimated delays from playing out each gradient waveform individually and in appropriate pairs for each plane orientation, are given in Table 4.1.

	X Gradient Delay (μs)		Y Gradient Delay (μs)		Z Gradient Delay (μs)	
	Single Gradient	Both Gradients	Single Gradient	Both Gradients	Single Gradient	Both Gradients
XY plane	-1.71	-1.69	-3.79	-3.78	–	–
XZ plane	-1.67	-1.7	–	–	-4.62	-4.58
YZ plane	–	–	-3.76	-3.77	-4.51	-4.46

Table 4.1: Gradient delay measurements made on a line phantom. For each gradient axis, results are provided for both single gradient and dual gradient acquisitions for two scan planes.

DISCUSSION

Experimental results for the zoom gradients on the 3T GE Signa Excite scanner (Table 4.1) show that the measured delays from gradient pairs closely follow those from individual gradients. This suggests that, for spiral scans on this scanner, delay on a gradient channel is not substantially influenced by the other two gradient channels.

The whole experiment requires a minimum of 16 $T_r s$ with more $T_r s$ improving the SNR of the acquired data. It is recommended that the whole experiment be carried out at least once to check for indication of gradient coupling. If there are no indications of coupling, the delay estimates from individual gradients (27) will be sufficient. Measurements on individual gradients require a minimum of just 6 $T_r s$. The placement of the phantom as described above is currently painstaking. This can be remedied by constructing a MR friendly phantom positioning jig that can be snapped into place in the receiver coils with help of slots/grooves.

Correcting for the delays can be implemented either during data acquisition or during reconstruction. Correction during data acquisition entails shifting the gradient waveforms by the negative of the measured delay, while correcting during reconstruction requires the k-space locations used during gridding and sampling density correction to be shifted by the measured delay. In either case, the gradient waveforms or the k-space trajectory need to be re-sampled, and a simple linear

interpolation was found to be adequate. Due to the simplicity of implementation, correction during reconstruction was adopted for this study.

The accuracy of the measured delays is about $0.5\mu s$ (27). The delays do not account for all gradient system imperfections. A more thorough approach would be to measure the played out k-space trajectory but requires prohibitively long scan times. Image reconstruction accounting for these delays eliminate approximately two-thirds of the total root-mean-square error resulting from k-space coordinate discrepancies for the MR system and spiral sequence used in this study (27).

SUMMARY

This work presents a simple algorithm to measure gradient coupling (if any) for the spiral trajectory. No major redesign of the trajectory or pulse sequence is required. The required line phantom is readily constructed from easily available material.

Experimental results for the spiral trajectories on the gradient system and scanner used in this study, suggest that the gradient channels have negligible effect on the delay in other gradient channels.

Chapter 5

SPIRAL DE-BLURRING

An important design specification of a MR system is the static external field (B_0) it can generate. This gives the system a characteristic resonant frequency ω_0 as determined by the Larmor equation. The signal receivers of the system are tuned to this frequency. This also is the base/carrier frequency used to induce nuclear resonance with a RF pulse. Any deviation from ω_0 is known as off-resonance and results in blurring the acquired images. The greater the off-resonance, the greater the blurring. Off-resonance can vary spatially; hence, the resulting blur is also a spatially varying artifact.

The complexity of the induced blurring depends on the k-space trajectory used to acquire the image. The effect in Cartesian scans is less complex compared to those on non-cartesian scans like spiral scans. The following sections provide an in-depth coverage of off-resonance, its effects, and approaches to controlling the resulting artifacts.

BASICS OF OFF-RESONANCE

The leading cause of off-resonance is the B_0 in-homogeneity (7, 9) – the spin system being imaged experiences a deviation in the effective external magnetic field and, hence, have an on-resonant frequency that differs from the system's expected Larmor frequency.

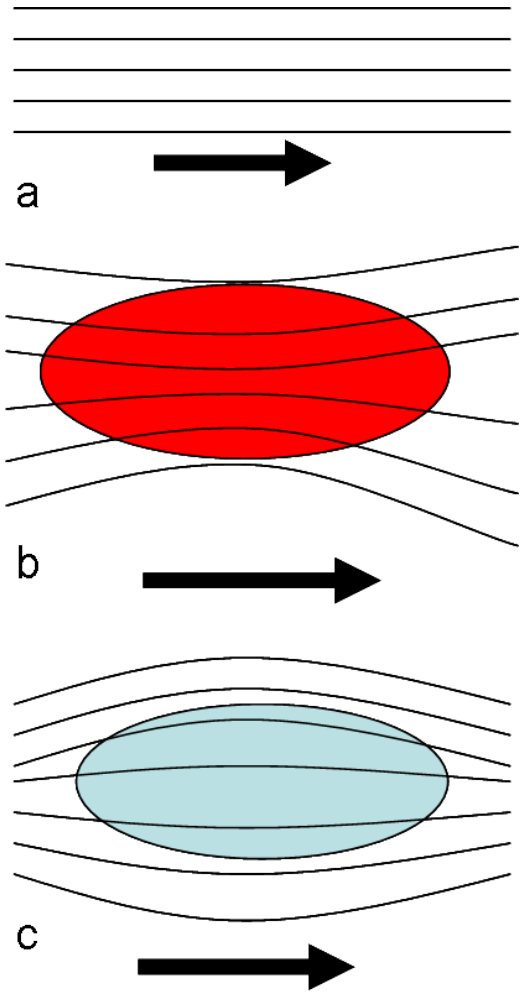

Figure 5.1: Flux lines for a homogeneous B_0 field (a). Flux lines for para-magnetic substance (b). Flux lines for dia-magnetic substance (c).

Though manufacturing tolerance may result in B_0 in-homogeneity, the dominating source is the sudden changes in the magnetic properties of the object being imaged. In particular, for brain imaging, the transitions from air to tissue around the nasal cavities generate severe in-homogeneity. Air is para-magnetic : it tends to strengthen the external magnetic field locally, while hydrogen the major constituent

of human tissue is dia-magnetic : it tends to weaken the external magnetic field locally. Figure 5.1a shows flux lines for an ideal homogeneous field, while Fig. 5.1b and Fig. 5.1c show the effects of para-magnetism and dia-magnetism, respectively. Since these air-tissue and tissue-tissue interfaces are characteristic of the object, the B_0 in-homogeneity is object dependent.

Mathematics of Imaging with Off-Resonance

In MR imaging, only the component of the magnetic moment in the transverse plane can be measured; for notational convenience, this is represented as $m(x)$. Let $M(k_x)$ be the Fourier transform of $m(x)$ and let $S(k_x;t)$ be the raw acquired signal. Though the treatment that follows is for one-dimensional signals, it can be easily extended to 2 and 3 dimensions. The effective magnetic field experienced by the spins is

$$B_{eff} = B_0 + \Delta_B(x) + G_x x \qquad [5.1]$$

where $\Delta_B(x)$ is the total deviation in magnetic field at x, and G_x (G/cm) is the spatial encoding gradient (a static auxiliary magnetic field along B_0 with a magnitude that varies linearly with x). Using the Larmor equation, we have the precession frequency as

$$\omega'_{eff} = \omega_0 + \Delta_\omega(x) + \gamma G_x x \qquad [5.2]$$

As ω_0 is the base/carrier frequency for signal detection, it can be ignored, resulting in

$$\omega_{eff} = \Delta_\omega(x) + \gamma G_x x \qquad [5.3]$$

The phase φ acquired by $m(x)$ in time dt' is given by

$$\varphi = \omega_{eff} dt' \qquad [5.4]$$

Now, ϕ the total phase acquired by $m(x)$ at time t is given by

$$\phi = \int_{t_0}^{t} \varphi = \int_{t_0}^{t} \omega_{eff} dt' \qquad [5.5]$$

where t_0 is the time instant at which data acquisition began. As $\Delta_\omega(x)$ is static (time-invariant)

$$\phi = \int_{t_0}^{t} \omega_{eff} dt' = \Delta_\omega(x)(t - t_0) + \gamma x \int_{t_0}^{t} G_x dt' \qquad [5.6]$$

$$\phi = \Delta_\omega(x)(t - t_0) + x k_x(t) \qquad [5.7]$$

Therefore, $m(x)$ acquires a phase ϕ at time t.

The measured value of the raw acquired signal at time t is the sum of $m(x)$ over all x and is given by

$$S(k_x;t) = \int_x m(x) e^{-j2\pi\phi} dx = \int_x m(x) e^{-j2\pi(\Delta_\omega(x)(t-t_0) + x k_x(t))} dx \qquad [5.8]$$

If $\Delta_\omega(x) = 0$ or the magnetic field is homogeneous, then the measured signal $S(k_x;t)$ is the Fourier transform of $m(x)$

$$S(k_x;t) = \int_x m(x)\, e^{-j2\pi(k_x(t))x} dx \qquad [5.9]$$

The Nature of Off-Resonance and its Effects

$\Delta_\omega(x)$ can be spatially invariant, vary linearly or non-linearly in the spatial domain. The resulting blurring has characteristic forms and is called zeroth, first and higher order effects, respectively. If $\Delta_\omega(x)$ is spatially invariant, then $\Delta_\omega(x) = \Delta_0$ and

$$\begin{aligned} S(k_x;t) &= \int_x m(x)\, e^{-j2\pi(\Delta_0(t-t_0)+xk_x(t))} dx \\ &= e^{-j2\pi\Delta_0(t-t_0)} \int_x m(x)\, e^{-j2\pi(k_x(t))x} dx \\ &= e^{-j2\pi\Delta_0(t-t_0)} M(k_x) \end{aligned} \qquad [5.10]$$

This shows that zeroth order effects generate a superfluous linear phase in k-space along the trajectory.

For $\Delta_\omega(x) = \Delta_0 + \Delta_1 x$ (linearly varying in the spatial domain),

$$\begin{aligned} \phi &= (\Delta_0 + \Delta_1 x)(t - t_0) + xk_x(t) \\ &= \Delta_0(t - t_0) + x\{\Delta_1(t - t_0) + k_x(t)\} \\ &= \Delta_0(t - t_0) + xk_x'(t) \\ S(k_x;t) &= \int_x m(x)\, e^{-j2\pi\phi} dx \end{aligned} \qquad [5.11]$$

Not only is a linear phase introduced to the collected data, the trajectory is also distorted. Figure 5.2 depicts the artifacts for Cartesian scans; these effects are manifested as geometric distortions – zeroth order effects as shifting in spatial domain,

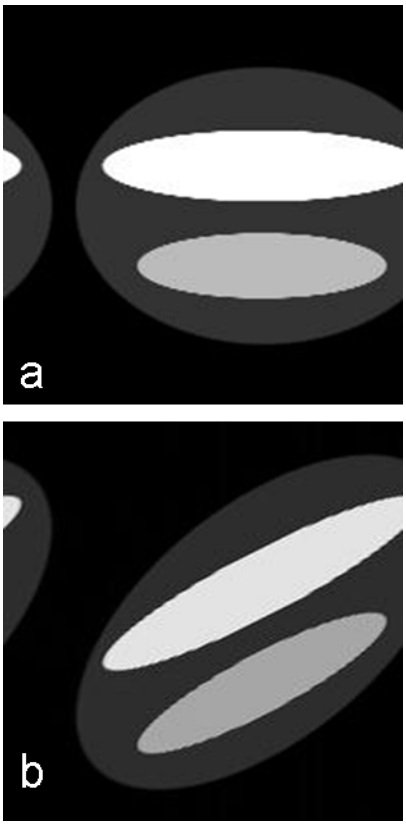

Figure 5.2: Cartesian scan with zeroth order effects (a) and with first order effects (b).

and the first order effects add rotation increasing in the direction of the trajectory in the spatial domain.

The effects on a spiral scan are more complex. Figure 5.3 shows the zeroth order effects, while Fig. 5.4 shows the distortion of trajectory due to the first order effects. An algebraic formulation of the effects has been given by (28).

A Measure of Blur in an MR Image

All the literature cited in this study use the Point Spread Function (PSF) to quantify the blurring. PSFs for spiral scans at different values of zeroth order off-resonance

Figure 5.3: An example of blurring in a spiral scan.

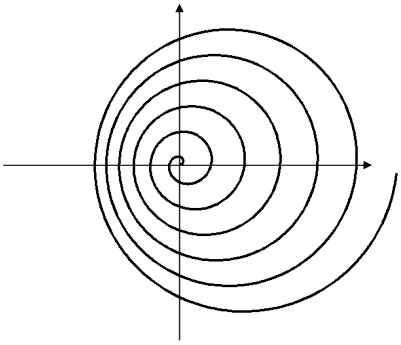

Figure 5.4: Spiral trajectory distortion due to first order effects.

are shown in Fig. 5.5. It can be easily observed that the PSF is increasingly distorted with greater off-resonance, but the region of support of the PSF is always finite.

Measuring the Local Resonant Frequency

Many of the de-blurring algorithms described in this study require an accurate map of the off-resonance in the spatial domain. This map is often referred to as the field map, frequency map, off-resonance map or the Local Resonant Frequency (LRF) map.

The field map is usually estimated using two images that are collected at differ-

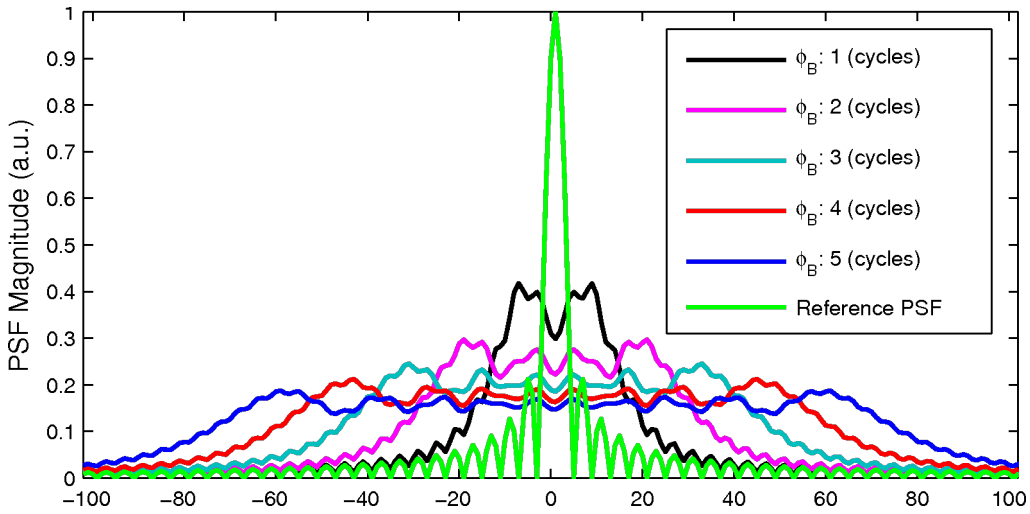

Figure 5.5: Blurred PSFs.

ent echo times. The off-resonance at some point is given by the ratio of the phase difference between values at that point and the difference in echo times. Care needs to be taken while evaluating the phase difference to account for the phase warping. Both gradient echo (29, 30, 31) and spin echo sequences (32, 33) can be used for this purpose.

Spatial Characteristics of the Field Map

Figure 5.6 depicts an actual field map, demonstrating the spatial dependence of the field map. Further, a majority of de-blurring algorithms assume that the field map varies slowly, i.e., the image can be segmented into finite regions each with zeroth order blurring at different values. Figure 5.7 shows a series of images with simulated blurring and which are de-blurred to correct for zeroth order effects at different values. As the de-blurred images clearly show, different parts of the image come

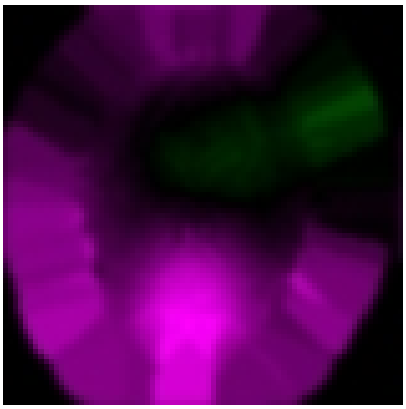

Figure 5.6: An example field map.

into focus as the value of the zeroth order off-resonance is varied. This indicates that the field maps may be assumed to be varying slowly. This demonstration is only an informal validation of the assumption that field maps vary slowly; a more rigorous proof can be found in the literature (34, 35).

De-Blurring Algorithms: A Review

Modern scanners have shim coils to help generate uniform fields (31); however, these coils are designed to compensate only for large global variations in the main magnetic field (17). This accounts for partial in-homogeneity corrections, necessitating further processing.

Till the mid 1990s, the most popular MR imaging schemes were the spin-warp imaging (10), 2DFT (10), projection reconstruction (PR) (10) and echo planar imaging (EPI) (10). It is thus natural that studies in this period concentrated in developing correction schemes for these imaging techniques. One of the earli-

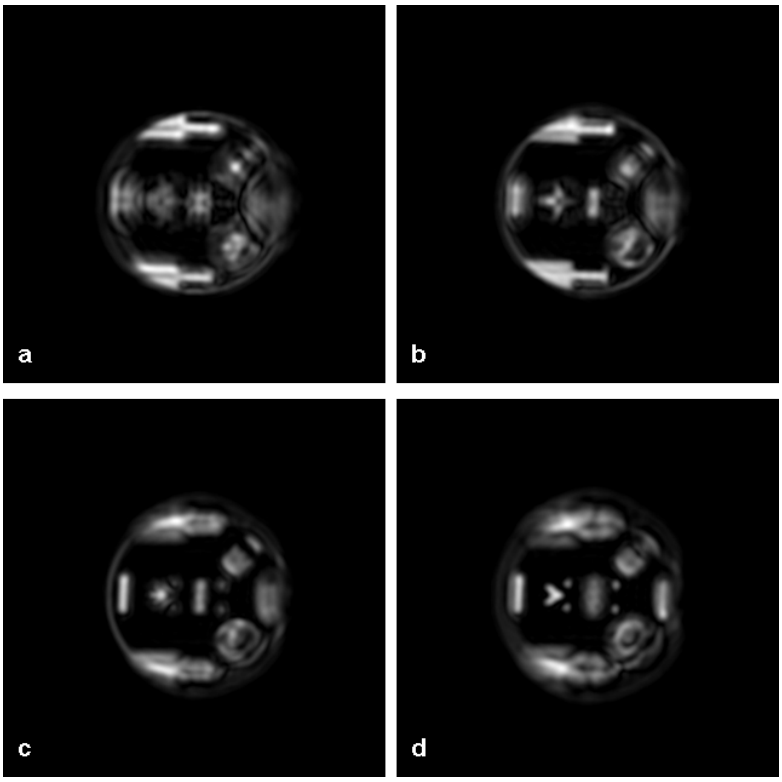

Figure 5.7: A blurred image (a) de-blurred at -15 Hz (b), -30 Hz (c), and at -45 Hz (d).

est approaches to handle artifacts due to B_0 in-homogeneity in post-processing for 2DFT imaging was published in 1978 (36). It was only in 1985 that a scheme that could correct for all effects (shifting and geometric distortions) of in-homogeneity in a 2DFT scan was proposed (33, 37). The algorithm involved a two-step approach. First, the shifting due to the zeroth order effects was handled by linear interpolation. This was followed by an algebraic approach to correct for geometric distortions. This algorithm is also applicable to variations of the EPI scan (38). A curvilinear reconstruction to correct for these effects in a PR scan had already been

described by Lai (39). Spin-warp imaging was found to be comparatively immune to blurring (40). A good review and comparison of these methods can be found in (41). A major contribution of these studies to de-blurring spiral scans and other non-cartesian scans has been the development of field map estimation techniques.

Algorithms for de-blurring spiral scans fall into three broad categories – the conjugate phase reconstruction (CPR) methods, the image space approaches and the automatic methods. The following sub-sections give an overview of these techniques.

Conjugate Phase Reconstruction

Conjugate phase reconstruction was introduced in 1988 (34). However, the term conjugate phase was coined by Noll (42) who also gave a more general form of the method. It is the standard method to correct for blurring. As shown before, the collected data in the presence of in-homogeneity is given by

$$s(t) = \int m(r) e^{[-ik(t)r - i\Delta_\omega(r)t]} dr \qquad [5.12]$$

Assuming a slow varying field map, $m(r)$ can be recovered by compensating for phase accrual via synchronously demodulating the collected signal at each point using the field map. Mathematically, this process can be represented as

$$\widehat{m}(r) = \sum_j s(t_j) e^{i\Delta_\omega(r)t_j} C(j,r) \qquad [5.13]$$

where $C(j,r)$ is a complex weighting function given by $C(j,r) = e^{[ik(t_j)r]} w(j)$. Here $w(j)$ is the sampling density correction weights (21). The name conjugate

phase reconstruction follows as each collected data point is multiplied by the conjugate of the accrued in-homogeneity phase.

A slightly variation to this process gives the SPHERE (Simulated PHase Evolution REwinding) reconstruction (43). SPHERE is a two step process – an estimate of the image space is obtained by standard reconstruction of the collected data. A corrected estimate of k-space is then obtained as

$$s_c(t) = \int \widetilde{m}(r) e^{[-ik(t)r + i\Delta_\omega(r)t]} dr \qquad [5.14]$$

The corrected image is then obtained by a standard reconstruction of the above. This can be iterated to improve the accuracy of correction.

Time Segmentation

Though reconstruction as formulated in Eq. 5.14 is possible, it is computationally intensive. A time segmented approach to speed up compensation was also proposed by Noll (42). The data is windowed into $L+1$ sets according to the collection time t_j. If the read out time is T, the windows are centered at $\tau = T/L$ and are 2τ wide. Each segment is separately reconstructed, corrected and summed to give the final image. Mathematically, this is equivalent to

$$\widehat{m}(r) = \sum_{l=0}^{L} \left[\sum_j s\left(t_j\right) a\left(t_j - l\tau\right) e^{i\Delta_\omega(r)t_j} C(j,r) \right] \qquad [5.15]$$

where $a(.)$ is the windowing function. The speed up is possible by the approximation that the in-homogeneity correction term is nearly constant over the window.

Then the reconstruction is

$$\widehat{m}(r) = \sum_{l=0}^{L} e^{i\Delta_\omega(r)l\tau} \left[\sum_j s\left(t_j\right) a\left(t_j - l\tau\right) C(j,r) \right] \qquad [5.16]$$

Here $l\tau$ is the center of the window. The reconstruction for each window

$$\sum_j s\left(t_j\right) a\left(t_j - l\tau\right) C(j,r) \qquad [5.17]$$

is fast if the standard reconstruction is fast. As mentioned before, $C(j,r)$ is a weighting function given by

$$C(j,r) = e^{[ik\left(t_j\right)r]} w(j) \qquad [5.18]$$

where $w(j)$ is the sampling density correction weights (21) used in the gridding reconstruction (20).

Frequency Segmentation

Computational complexity of the CPR can also be controlled by segmenting the off-resonance frequency range (44). Here, the range of off-resonance frequencies is uniformly quantized and a base image is reconstructed for each frequency with correction for only the zeroth order effects. The final image is formed pixel by pixel – the value at any location is the average of the pixel values at that location of two base images with the closet off-resonance frequency. This approach has been extended such that the reconstructed pixel value is the weighted average of the pixel values of all base images (45). Both of these quantize the off-resonance frequencies

in a one dimensional manner, a better speed up can be achieved by quantizing in two dimensions (46).

Automatic Methods

All of the methods described above require an accurate field map. Generating a field map entails increased scan times and assumes that the field map is time invariant. In most applications, these constraints are satisfied. But, in applications like real-time cardiac and lung imaging, increased scan times are not desirable and the field map varies with time. For such cases, a class of methods that ”automatically” de-blur the images are attractive.

Use of a focusing measure to iteratively de-blur each image pixel (44) attempts automatic de-blurring by adopting a modified focusing measure from radio astronomy. The de-blurring then proceeds in the basic frequency segmented approach. The focusing measure is the sum of a nonlinear function of the imaginary parts of the pixel values around a predetermined area around the pixel. An extension of this approach to include support for a large range of sharply varying off-resonance frequencies has also been proposed (47) – the area of summation and the range of off-resonance frequencies are successively fine tuned until the required robustness is achieved.

Summary

As is evident from the above, CPR is the basis for all other classes of de-blurring methods. CPR is the continuous domain formulation of the problem, and each method attempts an optimal approximation by different approaches to discretization of the continuous formulation (Yudilevich *et. al* (28) give a thorough analytical treatment of the continuous formulation). A rigorous analysis of these methods with the development of the general form of each method has been made (48). The study indicates that frequency segmentation approaches provide the best approximation.

DE-BLURRING WITH SEPARABLE KERNELS

This technique was introduced (49) as a computationally fast alternative to the conjugate phase methods. It is a frequency segmented approach that is implemented in image space. It assumes that an accurate field map is available and that it varies slowly in image space. The image is first reconstructed with the basic gridding technique. The range of off-resonance frequencies is uniformly quantized and a de-blurring kernel is generated for each frequency. If f_i denotes an off-resonant frequency, then the de-blurring kernel is

$$I.F.T.\left\{\left(fit\left[MTF_{f_i}\right]\right)^{-1}\right\} \qquad [5.19]$$

where $I.F.T.$ is the inverse Fourier transform, MTF_{f_i} is the modulation transfer function given by the Fourier Transform of the point spread function, PSF_{f_i}, for a constant off-resonance f_i. Further, $fit[MTF_{f_i}]$ denotes modeling the MTF_{f_i} based

on the characteristics of the spiral trajectory. Usually, spiral trajectories are traversed with a constant linear velocity allowing t the acquisition time to be expressed as

$$t \propto k_x^2 + k_y^2 \qquad [5.20]$$

Since the phase accrual due to off-resonance is proportional to t, it can be modeled as a 2D separable quadratic, $e^{i(k_x^2+k_y^2)}$, making this approach computationally efficient.

A kernel table is first generated using the maximum off-resonance frequency in the field map. Each pixel in the corrected image is the result of two 1D (three if correcting 3D data-sets) convolutions with the kernel specified by the offset frequency at that pixel. Care is taken to ensure that the convolutions are centered on the pixel of interest. Figure 5.8 illustrates this graphically.

Sufficient Kernel Length

Visual inspection of a typical kernel table (Fig. 5.9) indicates that computation cost can be further reduced by using a varying kernel length. The kernels are Fourier transforms of the complex conjugate of the respective MTF_{f_i}; hence, the convolution of the blurred PSF and the associated kernel should ideally result in a sinc function. This gives a metric to measure the kernel performance as

$$ErrorMetric = \frac{\sum |PSF_c - PSF_i|^2}{\sum |PSF_i|^2} \qquad [5.21]$$

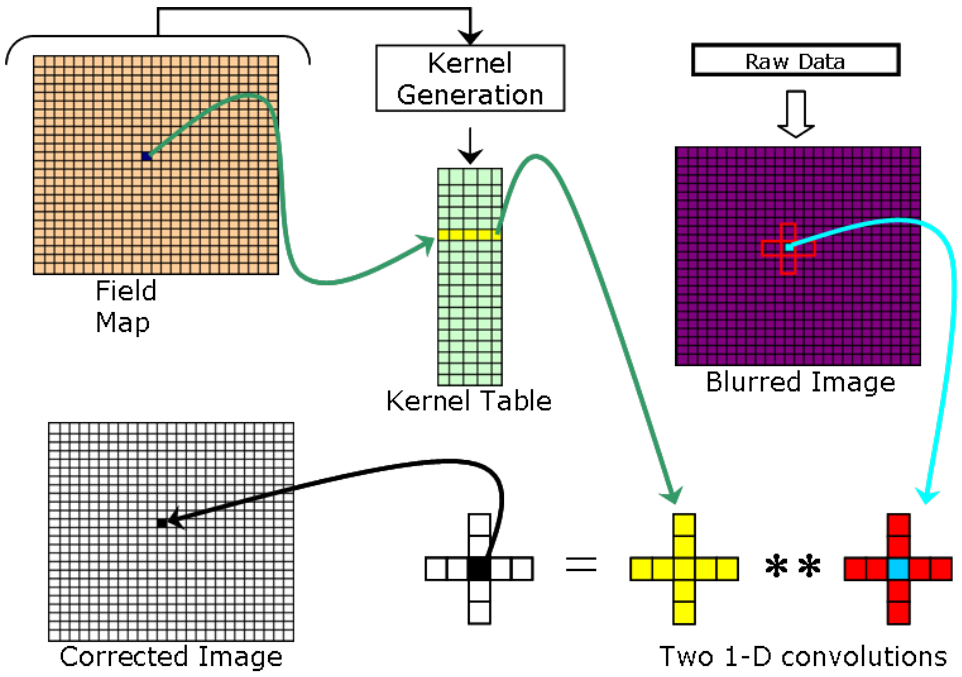

Figure 5.8: Flowchart for rapid 2D de-blurring via separable kernels.

where PSF_c is the de-blurred PSF and PSF_i the ideal sinc PSF. The kernel performance is expected to improve with increasing kernel length. This is demonstrated in Fig. 5.10 for a total phase accrual (ϕ_b) of 5 cycles. The kernel performance as a function of kernel length for $\phi_b = 1-10$ cycles is illustrated in Fig. 5.11 and, as expected, the performance improves with increasing kernel length. Since the amount of introduced blur is proportional to ϕ_b (Fig. 5.5), it is straightforward to anticipate that the sufficient kernel length is a function of ϕ_b. The kernel performance was tested for varying kernel lengths given by

$$\text{Kernel Length} = 2(4\phi_b + n) \qquad [5.22]$$

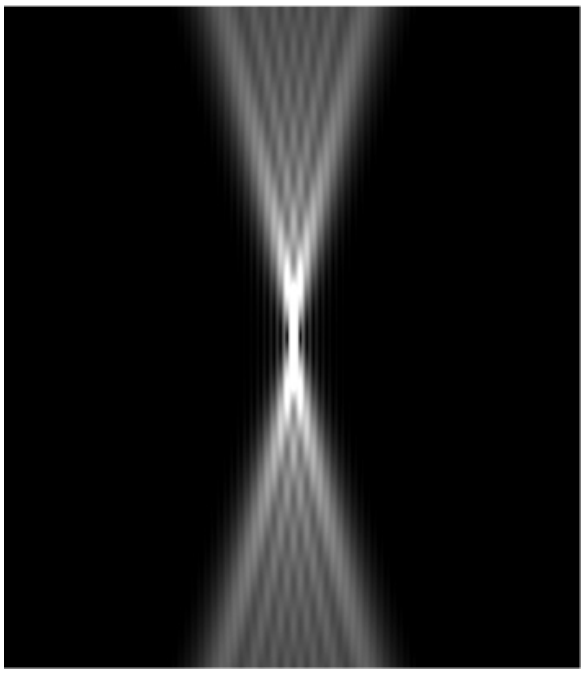

Figure 5.9: A typical kernel table exhibiting the bow tie structure indicating the variation in kernel length.

for $n = 0, 3, 20$. The results are superimposed on Fig. 5.11. In practice, a SNR of 100 is suffcient for most MR applications (50), i.e., any reduction in residual error beyond 10^{-2} level is lost. Figure 5.11 indicates that kernel lengths greater than $2(4\phi_b + 3)$ are not computationally efficient; hence, a kernel length given by $2(4\phi_b + 3)$ is *sufficient* for practically effective and computationally efficient deblurring.

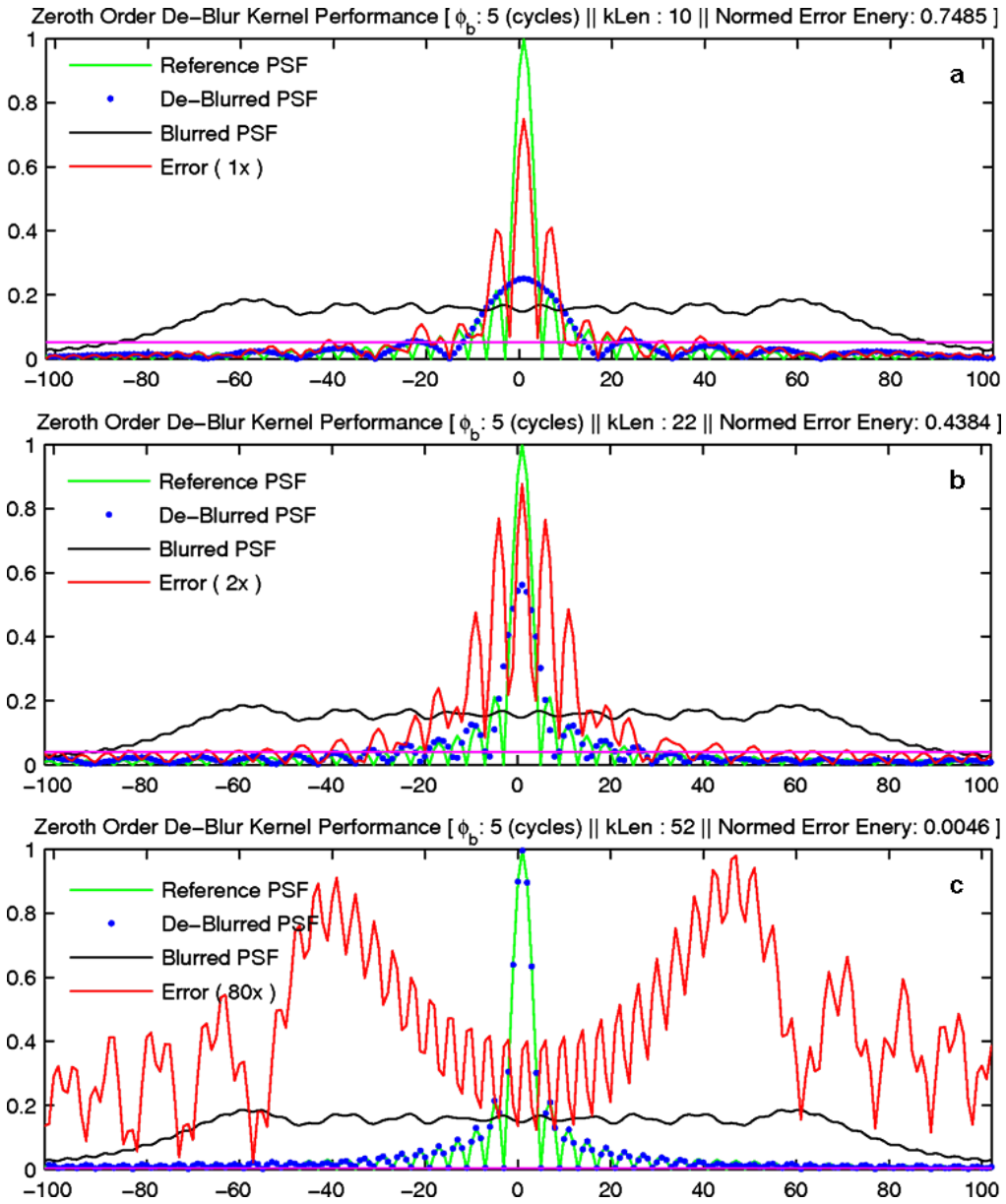

Figure 5.10: Kernel performance for $\phi_b = 5$ cycles with different kernel length : 10 (a), 22 (b), and 52 (c).

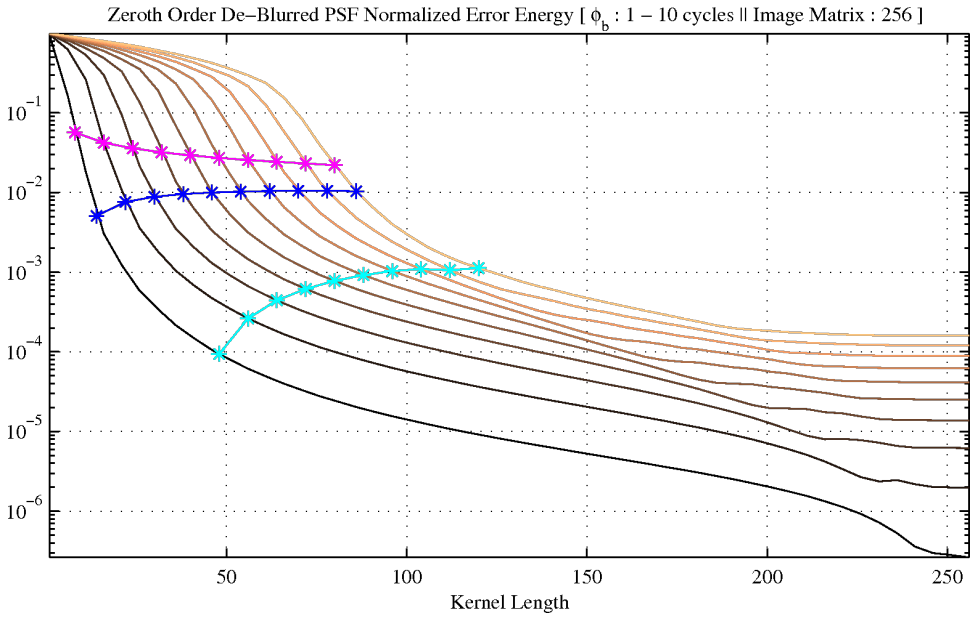

Figure 5.11: Kernel performance for different values of ϕ_b (1 - 10 cycles) as a function of kernel length (darker lines indicate lower values of ϕ_b and lighter lines indicate larger values). Performance results for kernel length given by Eq. 5.22 for $n = 0$ (magenta), $n = 3$ (blue), and $n = 20$ (cyan), are also superimposed.

Linear Field Map Correction

A linear variation in space of the field map (Δ_ω) can be accounted for by a first order term (Δ_1). In one dimension, this is represented as:

$$\Delta_\omega(x) = \Delta_0 + \Delta_1 x \qquad [5.23]$$

The presence of Δ_1 is equivalent to a spurious gradient during spatial encoding (Eq. 5.11). For spiral scans, this manifests itself as a distortion in the trajectory (Fig. 5.4 and (51)). The trajectory distortion results in a change in sampling density. This discrepancy in sampling density can be estimated by density compensation algorithms (21). However, the trajectory distortion varies with each pixel, and estimating the

density compensation is computationally intensive. Hence, an analytical solution for estimating the change in sampling density is desired. This section presents a closed form solution based on the characteristics of the spiral trajectory.

Modeling the Change in Sampling Density

In accounting for the zeroth order effects, the acquisition time t was assumed to be (49) :

$$t = ck_r^2 \qquad [5.24]$$

where c is a constant scalar and $k_r^2 = k_x^2 + k_y^2$. For ease of presentation, the estimate of change in sampling density is first derived in one dimension, and then extended to multiple dimensions. Let k_i be the i-th undistorted k-space location and let K_i be the corresponding distorted k-space location. With both k_i and K_i normalized to ± 0.5, for a given spurious gradient G and resolution r, K_i can be expressed as

$$K_i = k_i + \gamma r G t_i \qquad [5.25]$$

Using Eq. 5.24, Eq. 5.25 can be rewritten as

$$K_i = k_i + \gamma r G c k_i^2 \qquad [5.26]$$

Let K_i^{Δ} be defined as

$$K_i^{\Delta} = (k_i + \Delta) + \gamma r G c \, (k_i + \Delta)^2 \qquad [5.27]$$

where Δ is the normalized Nyquist distance. For every K_i, K_i^{Δ} corresponds to the next k-space location that is acquired as specified by the original trajectory. By

definition, any change in sampling density at any location is given by the distance between adjacent sample locations scaled by the reference distance between adjacent sample locations, i.e., the Nyquist distance. Assuming that the distortion due to G does not cause the trajectory to fold over itself, $\left(K_i^{\Delta} - K\right)/\Delta$ is proposed as an estimate of the change in sampling density. From Eq. 5.26 and Eq. 5.27, the change in sampling density at K_i is

$$\delta\left(SD_i\right) = 1 + 0.5B\Delta + Bk_i \qquad [5.28]$$

with $B \stackrel{\Delta}{=} 2\gamma rGc$. Equation 5.26 can also be used to solve for k_i as

$$k_i = \left(-1 \pm \sqrt{1 + 2BK_i}\right)\Big/B \qquad [5.29]$$

Only the positive root will result in k_i between ± 0.5 giving

$$\delta\left(SD_i\right) = 0.5B\Delta + \sqrt{1 + 2BK_i} \qquad [5.30]$$

The constant c is specified by the analog to digital conversion (ADC) time (the duration of the data acquisition window) as, by definition, $k_{max} = 0.5$ is acquired at the end of the data acquisition window giving

$$c = 4ADC \qquad [5.31]$$

Since this treatment assumes that G does not cause the trajectory to fold over, it is necessary to determine the critical value (G_c) at which G begins to cause the trajectory to fold over. G_c is given by the value of G for which $\delta(SD_i) = 0$ at

$k_i = -k_{max}$. Using $-k_{max} = -0.5$ in Eq. 5.28, we get

$$G_c = [\gamma rc\,(1-\Delta)]^{-1} \qquad [5.32]$$

Since the trajectory distortion results in a change in sampling density, the compensation that is needed to correct for the trajectory distortion is a multiplication in k-space by the inverse of the change in sampling density, i.e., the kernel magnitude in k-space needs to set as

$$|\text{kernel}_{\text{MTF}}| = [\delta\,(SD_i)]^{-1} \qquad [5.33]$$

To ensure that the kernel is separable in two dimensions, Eq. 5.30 can be linearized using a Maclaurin series expansion (52) and by setting the high order terms of the expansion to zero

$$|\text{kernel}_{\text{MTF}}| = [1 + BK_i]^{-1} \qquad [5.34]$$

with $G \leq 0.45 G_c$.

Efficacy of the First Order De-Blur Kernels

The first order de-blur kernel design follows that for zeroth order kernels – the phase is the conjugate of the phase accrual in k-space, and the magnitude in k-space is now specified by Eq. 5.33. The value of B is determined by the change in total phase accumulated per pixel ($d\phi_b$ in units of cycles per pixel) as

$$B = 8\,d\phi_b \qquad [5.35]$$

$d\phi_b$ (centi-cycles per pixel)	1	2	3	4	5	6	7	8	9
Percent Improvement	29	36	38	38	38	37	36	35	33

Table 5.1: Improvements in correcting for a linear field map using a first order kernel in comparison to a zeroth order kernel.

The result in one dimension is shown in Fig. 5.12 for typical values of ϕ_b and $d\phi_b$ with and without non-uniform magnitude. The percent improvement was computed as

$$\text{Percent Improvement} = \left(\frac{Error_{\text{zeroth order kernel}} - Error_{\text{first order kernel}}}{Error_{\text{zeroth order kernel}}} \right) \times 100 \qquad [5.36]$$

Table 5.1 lists the percent improvement for various values of $d\phi_b$.

Sufficient First Order Kernel Length

The kernel length computed using Eq. 5.22 with $n = 3$ has to be verified for first order kernels. Figure 5.13 plots the residual error after first order correction for different values of $d\phi_b$ as a function of zeroth order sufficient kernel length. The

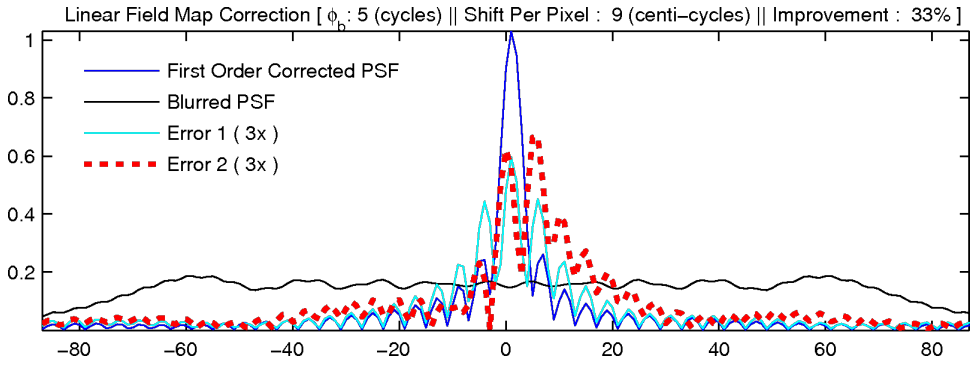

Figure 5.12: First order kernel performance in comparison to the zeroth order kernel. The first order residual error (Error 1) is 33 percent less than the zeroth order residual error (Error 2).

achieved error values indicate that the kernel length given by Eq. 5.22 with $n = 3$ is indeed sufficient.

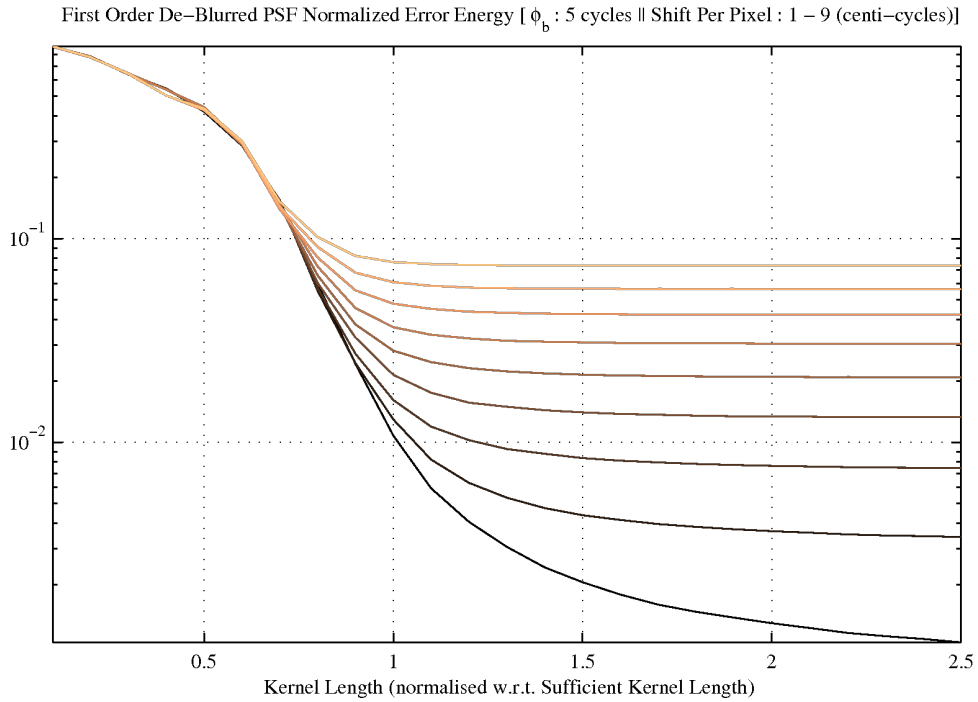

Figure 5.13: First order kernel performance as a function of kernel length computed using Eq. 5.22 with $n = 3$.

NOISE CHARACTERISTICS

De-blurring with separable kernels is essentially a deconvolution technique. Deconvolution approaches are generally sensitive to noise. A Monte-Carlo simulation was used to investigate the noise characteristics of de-blurring with separable kernels. The blurred *PSF* is corrupted with N instants of zero-mean white Gaussian noise (the variance was as per the required SNR) and then de-blurred with the associated kernels. Figure 5.14 depicts this procedure graphically. The standard deviation (σ)

of each pixel, the mean deviation of each value from the average value of the pixel across the N versions of the PSF, is then computed pre- and post-correction. For good noise characteristics, pre- and post-compensation σ values need to be comparable.

The results for zeroth order correction (Fig. 5.15) indicates that the pre- and post-correction σ values are indeed comparable implying good noise performance. For first order correction the pre- and post-correction σ are comparable till 9 centi-cycles per pixel shift (Fig. 5.16a), after which there is noise amplification (Fig. 5.16b). The spurious first order gradient G results in different phase accumulation at each pixel which is specified in cycles per pixel shift. Usually this per pixel shift is on the order of 0.01 cycles hence the use of centi-cycles for ease in presentation. This is expected as the magnitude of the kernel MTF is no longer constant (Eq. 5.34). Whether this is acceptable in practice depends on the SNR of the image being corrected. The fall in post-correction σ values towards the edges are due to partial convolutions effects (as indicated by the asymmetric nature in the first order kernel result shown in Fig. 5.16).

Concomitant Field Correction

Imaging gradients necessary for spatial encoding also generate unintended additional spatially varying magnetic fields. Though these concomitant fields (B_c) are inadvertent, they are not due to any hardware imperfections. In reality, they are

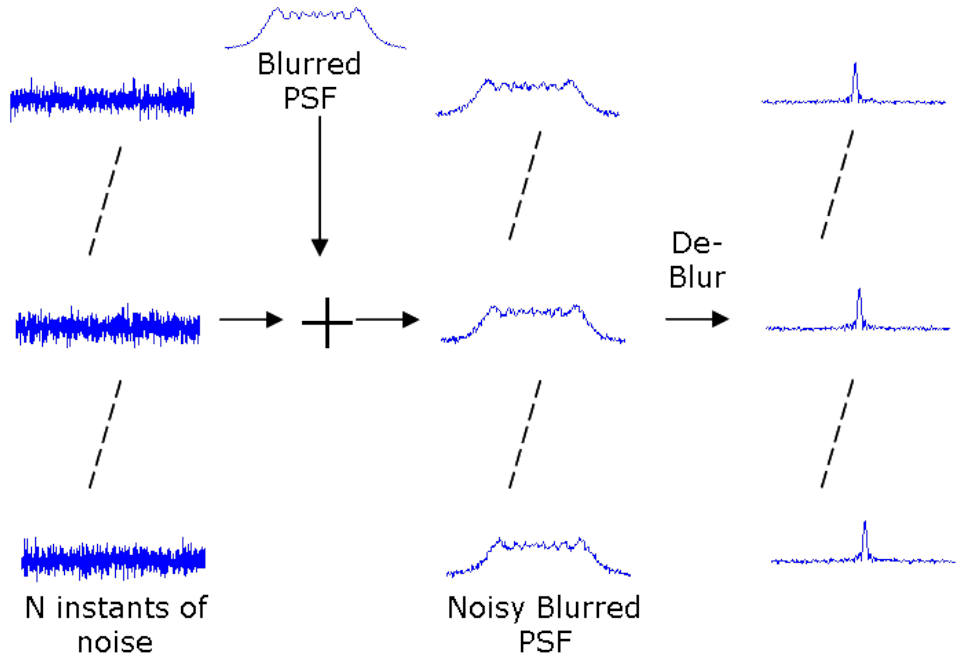

Figure 5.14: Graphical representation of the Monte Carlo procedure adopted for investigating the noise performance of the de-blurring via separable kernels.

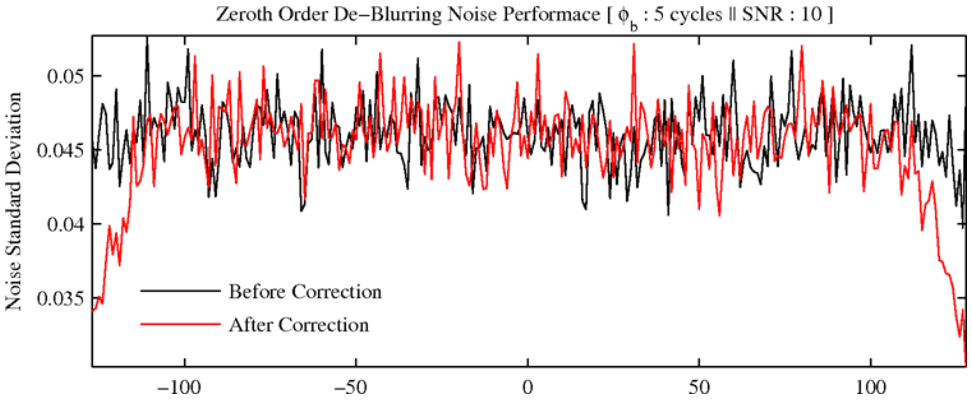

Figure 5.15: Noise performance of a typical zeroth order kernel.

predicted by Maxwell's equations and hence unavoidable. The nature of their occurrence precludes any attempts to measure them. Fortunately, closed form first order approximations using the Maxwell equations can be derived (8, 53). This

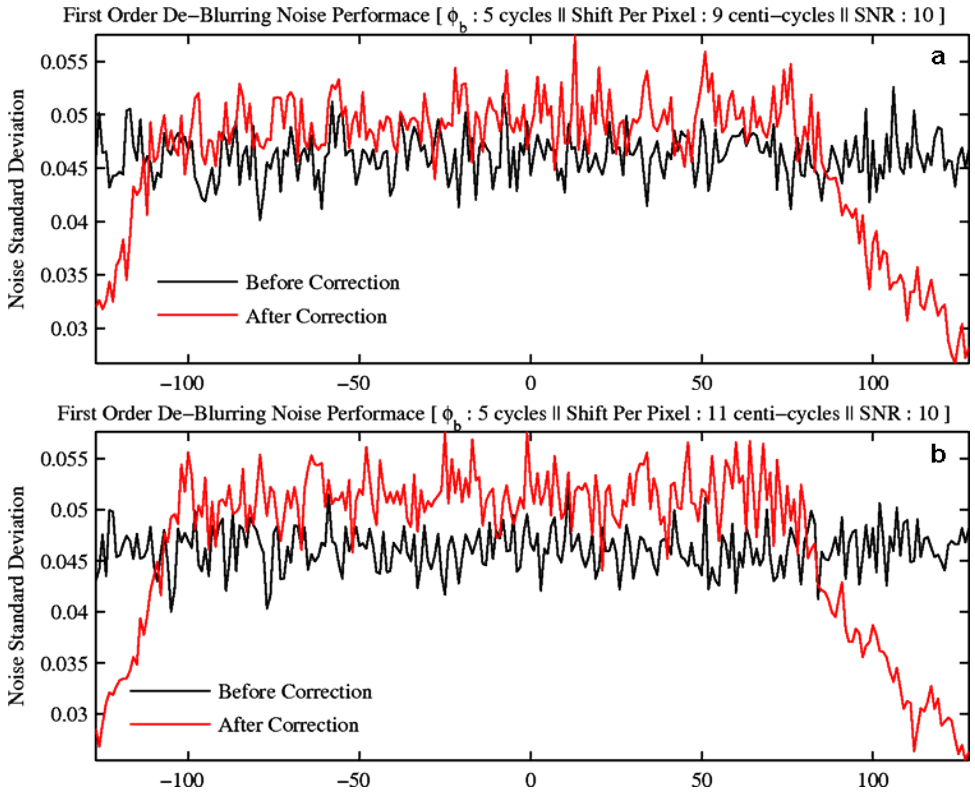

Figure 5.16: First order kernel noise performance for 9 centi-cycles per pixel shift (a), and 11 centi-cycles per pixel shift (b).

can be demonstrated succinctly for a constant gradient along the x-direction (G_x). Maxwell equations for magnetic fields state:

$$\begin{aligned} \overrightarrow{\nabla} \bullet \overrightarrow{B} &= 0, \\ \tfrac{1}{\mu_0} \overrightarrow{\nabla} \times \overrightarrow{B} &= \varepsilon_0 \tfrac{\partial \overrightarrow{E}}{\partial t} + \overrightarrow{J}. \end{aligned} \qquad [5.37]$$

where $\overrightarrow{\nabla}$ is the derivative operator, $\overrightarrow{E}$ the electric field, $\overrightarrow{J}$ the current density, μ_0 the permeability, and ε_0 the permittivity of free space. For an MRI scanner, $\partial \overrightarrow{E} / \partial t \approx 0$ and $\overrightarrow{J} \approx 0$ (8), giving:

$$\frac{\partial B_x}{\partial x} + \frac{\partial B_y}{\partial y} + \frac{\partial B_z}{\partial z} = 0 \qquad [5.38]$$

$$\frac{\partial B_x}{\partial y} = \frac{\partial B_y}{\partial x} \quad [5.39]$$

$$\frac{\partial B_y}{\partial z} = \frac{\partial B_z}{\partial y} \quad [5.40]$$

$$\frac{\partial B_z}{\partial x} = \frac{\partial B_x}{\partial z} \quad [5.41]$$

By definition, $\partial B_z/\partial x = G_x$, $\partial B_z/\partial y = G_y$ and $\partial B_z/\partial z = G_z$. Let $G_\perp$ be a transverse gradient defined as

$$G_\perp \triangleq \frac{\partial B_x}{\partial y} = \frac{\partial B_y}{\partial x} \quad [5.42]$$

Equation 5.38 specifies $\partial B_x/\partial x$ and $\partial B_y/\partial y$ as

$$\begin{aligned} \tfrac{\partial B_x}{\partial x} &\triangleq -\alpha G_z \\ \tfrac{\partial B_y}{\partial y} &\triangleq -(1-\alpha) G_z, \end{aligned} \quad [5.43]$$

where α is a dimensionless parameter. $\overrightarrow{B}$ is a spatially varying vector and can be linearized as:

$$\begin{bmatrix} B_x \\ B_y \\ B_z \end{bmatrix} = \begin{bmatrix} \frac{\partial B_x}{\partial x} & \frac{\partial B_x}{\partial y} & \frac{\partial B_x}{\partial z} \\ \frac{\partial B_y}{\partial x} & \frac{\partial B_y}{\partial y} & \frac{\partial B_y}{\partial z} \\ \frac{\partial B_z}{\partial x} & \frac{\partial B_z}{\partial y} & \frac{\partial B_z}{\partial z} \end{bmatrix} \begin{bmatrix} x \\ y \\ z \end{bmatrix}. \quad [5.44]$$

Here, B_z refers to only the spatially varying component. Using Eq. 5.40 - Eq. 5.43 and the assumption that only a constant linear gradient along the x-direction exists, Eq. 5.44 reduces to

$$\begin{bmatrix} B_x \\ B_y \\ B_z \end{bmatrix} = \begin{bmatrix} 0 & G_\perp & G_x \\ G_\perp & 0 & 0 \\ G_x & 0 & 0 \end{bmatrix} \begin{bmatrix} x \\ y \\ z \end{bmatrix} \quad [5.45]$$

MRI scanners use cylindrical gradients; consequently, $G_\perp \approx 0$ (8), giving

$$\begin{aligned} B_x &= G_x z \\ B_z &= G_x x \end{aligned} \qquad [5.46]$$

Equation 5.46 clearly demonstrates that a linearly varying magnetic field in one direction generates an additional magnetic field perpendicular to the original field.

Derivation for the more general case follows the procedure outlined above giving the first-order approximation of the generated concomitant field B_c for a general 3D gradient waveform as (53):

$$B_c = \left(\frac{g_z^2}{8B_0}\right)\left(x^2+y^2\right) + \left(\frac{g_x^2+g_y^2}{2B_0}\right)z^2 - \left(\frac{g_x g_z}{2B_0}\right)xz - \left(\frac{g_y g_z}{2B_0}\right)yz \qquad [5.47]$$

Equation 5.47 has been shown to be an adequate estimate of concomitant fields for correction (53, 54).

Rapid Concomitant Field Correction

Variations in the effective B_0 due to the concomitant fields will also result in additional phase accrual in k-space during spatial encoding. This additional phase ($\Phi_c(t)$) is given by:

$$\Phi_c(t) = \gamma \int_0^t B_c(\tau)\, d\tau. \qquad [5.48]$$

The effect of $\Phi_c(t)$ on image quality is similar to B_0 in-homogeneity. It has been demonstrated (54) that traditional de-blurring algorithms for spiral trajectories can be modified to account for the effects of concomitant fields. Traditional de-blurring algorithms are, however, handicapped by long computation times. An investigation

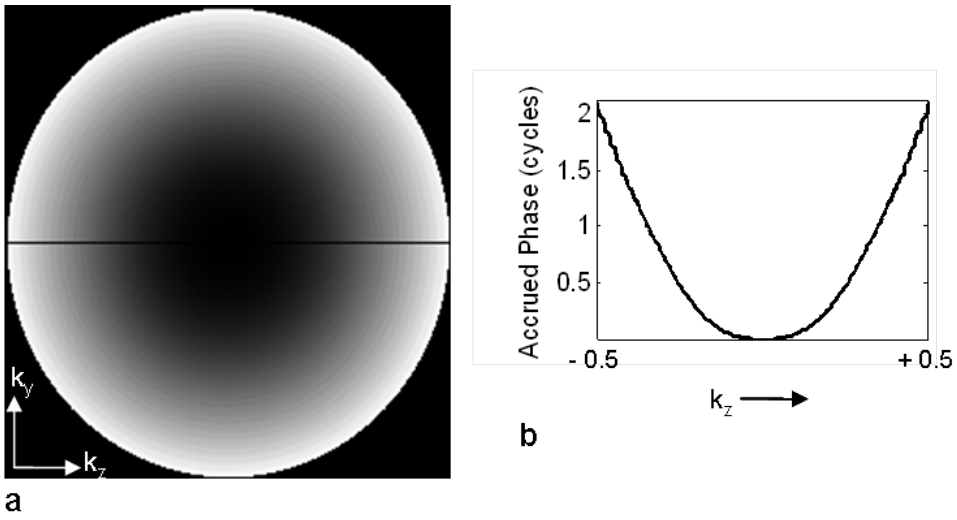

Figure 5.17: The phase accrual in k-space for a single pixel with a typical sagittal spiral scan (a). The profile through the origin (b) clearly illustrates the quadratic nature of the accrual. The trajectory had 4 interleaves, G_{max} of 4 G/cm and *ADC* of 42.5 ms. The pixel location was assumed to be x = 2cm, y = 2cm and z = 12cm.

of the phase accrual in k-space from Eq. 5.48 for a typical spiral trajectory reveals that it is approximately quadratic (Fig. 5.17). This is fortuitous as a quadratic phase accrual in k-space can be corrected rapidly using separable de-blur kernels (49).

Though the separable de-blur kernel approach is rapid, it still requires a time-independent field map. As is evident from Eq. 5.47, the expression for concomitant fields is time-dependent. The quadratic phase accrual again provides the work around, as each pixel can now be assumed to have an off-resonance frequency ($\Delta f_c\,(x,y,z)$) given by

$$\Delta f_c\,(x,y,z) = \frac{\text{Max Phase Accrual for pixel at}(x,y,z)\,(\Phi_c^{\max}(x,y,z))}{\text{ADC Time (T)}}. \qquad [5.49]$$

where $\Phi_c^{\max}$ is $\Phi_c(t)$ at $t =$ ADC Time, and ADC Time is the data acquisition win-

dow length. The resulting virtual field map is time-independent permitting the use of the rapid de-blurring algorithm.

Computing the Virtual Field Map

Computing the virtual field map directly from Eq. 5.49 is time consuming as Δf_c at every pixel is a summation of N terms ($N =$ # of acquired samples) (Eq. 5.48). The equation for maximum accrued phase after a rearrangement of terms can be rewritten as:

$$\Phi_c^{\max}(x,y,z) = \frac{\gamma}{2B_0}\left[\frac{(x^2+y^2)}{4}\int_0^T g_z(\tau)^2\,d\tau + z^2\int_0^T\left(g_x(\tau)^2 + g_y(\tau)^2\right)d\tau \right. \\ \left. -xz\int_0^T g_x(\tau)\,g_z(\tau)\,d\tau - yz\int_0^T g_y(\tau)\,g_z(\tau)\,d\tau\right] \qquad [5.50]$$

The four integrations do not vary with pixel location and need to be computed only once. Using these pre-computed summation values, $\Delta f_c(x,y,z)$ can be computed swiftly.

Validation in 2D

The proposed algorithm was validated with both simulation and phantom data. The original image for the simulation was acquired using a 240x240 image-matrix Cartesian spoiled gradient echo sequence. As indicated by Eq. 5.8, the simulation was computed by evaluating:

$$M(k_y,k_z) = \sum m(y,z)\,e^{i2\pi\left[yk_y(n)+zk_z(n)+\Delta f_c(y,z)\,t(n)\right]} \qquad [5.51]$$

The simulation trajectory was a 5-interleave Archimedean spiral designed for 24cm FOV, 1mm resolution and 4.00G/cm G_{max}. The x-offset was assumed to be 2 cm.

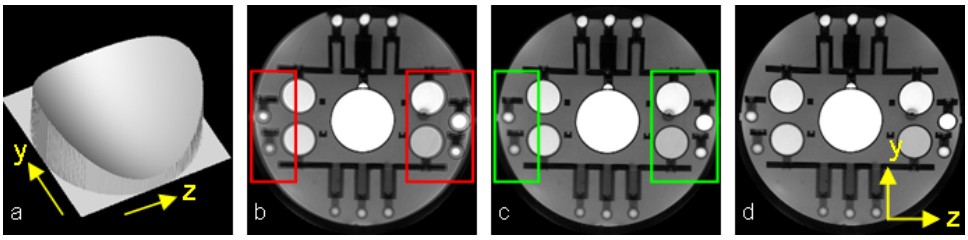

Figure 5.18: Concomitant field correction results for simulated sagittal images: virtual field map (a); uncorrected image (b); de-blurred image (c) and original image (d).

The phantom data was acquired on a 3T GE Signa Excite scanner with 150/40 gradient system. The acquisition trajectory was a 7-interleave Archimedean spiral designed for 22.4cm FOV, 1mm resolution and 2.25G/cm G_{max}. The sagittal slice had an x-offset of 1.2cm. To reduce the effect of B_0 in-homogeneities, 5 iterations of the high order shimming (to produce a uniform B_0 field) sequence that is provided by the scanner manufacturer, were carried out.

The raw data was reconstructed using standard gridding reconstruction (20) and sampling density correction (9). The reconstructed data was then de-blurred using the separable kernels (49).

The simulation trajectory resulted in an ADC time of 28 ms giving a maximum off-resonance frequency of 54 Hz. The computed virtual field map and the achieved de-blurring using separable kernels are shown in Figs. 5.18a-c; the original Cartesian image is also shown in Fig. 5.18d for reference. The trajectory for the phantom images also resulted in an ADC time of 28 ms but with a maximum off-resonance frequency of 21 Hz. The computed virtual field map and the achieved de-blurring

using separable kernels are shown in Figs. 5.19a-c, and magnified portions of the uncorrected and de-blurred images are also shown in Fig. 5.19d for easy comparison.

Discussion

The de-blurred images from both the simulation and the phantom experiments (Fig. 5.18c and Fig. 5.19d) clearly demonstrate the efficacy of the proposed method to correct for concomitant effects in spiral scans. The understated improvements in the phantom experiments are consistent with the smaller $\Delta f_c^{\max}$ (21 Hz as compared to 54 Hz in the simulations). The computed virtual field maps are also consistent

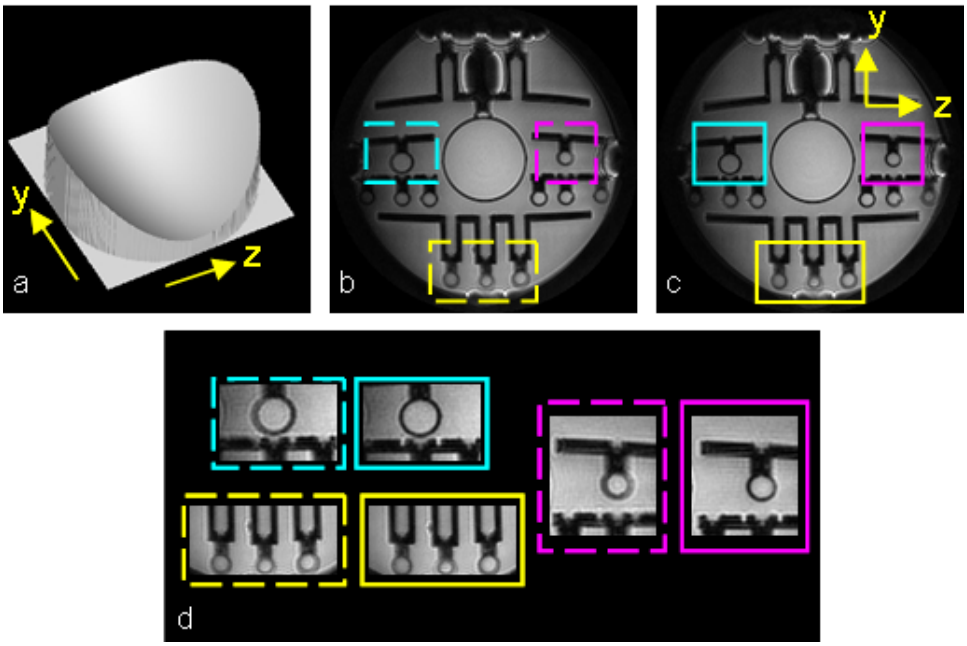

Figure 5.19: Concomitant field correction results for phantom sagittal images: virtual field map (a); uncorrected image (b) and de-blurred image (c) with the marked portions of both images zoomed-in (left: uncorrected image; right: de-blurred image) for easy comparison (d).

with Eq. 5.47 – increase in Δf_c is more aggressive along the z-direction than along the y-direction and, in both cases, the increase is quadratic. The quadratic relationship is explicitly visible along the z-direction. The raw phantom images also reflect the blurring predicted by Eq. 5.47 – blurring is more subtle along the vertical axis in comparison to the horizontal axis. The amount of correction depends on the accuracy of the virtual field map and the efficacy of the separable kernel algorithm.

The form of the proposed approach – using a static pre-computed virtual field map to correct for concomitant fields, has further potential computational advantages. The virtual field map can be combined with the B_0 field map (a simple addition should suffice) permitting correction for both artifacts simultaneously, effectively reducing the computation time by half. Past solutions (54) require a separate step for concomitant correction. This combined field map can also be used with other de-blurring techniques such as time segmentation (42) and frequency segmentation (44).

Empirical evidence suggests that the concomitant effects are not visible in all spiral scans (54). A closer look at Eq. 5.47 helps explain this – B_c effects decrease with increasing B_0, and increase with increasing maximum used gradient and increasing ADC time. Larger objects will also have larger B_c effects. Equation 5.47 also reveals that axial scans experience a constant off-resonance from concomitant fields. Solutions to correct for constant off-resonance are exceptionally efficient (both in terms of artifact elimination and computation time) even for spiral scans

(8). With the MRI industry moving towards 3T scanners and the possibility of de-rating the gradients, these factors seem to play down the effects of concomitant fields. For non-cartesian trajectories designed for fast coverage of k-space (implying long ADC times), concomitant field effects are a handicap and need to be corrected.

DE-BLURRING IN 3D

Non-cartesian 3D trajectories have certain undeniable advantages – fast scanning (typical scan times are just a third of that for Cartesian scans), benign aliasing patterns, potential 3D rigid body motion correction/robustness while preserving or exceeding the SNR performance of Cartesian scans. These attributes are compelling enough to warrant the development of algorithms for 3D spiral de-blurring.

Floret Trajectory

The floret is a recently introduced 3D trajectory based on spirals (55). Here the base spiral plane is under-sampled in-plane (Fig. 5.20a), then stretched out in the direction perpendicular to the plane (Fig. 5.20b). The stretching forms cones of different angles. A number of such base spirals form a hub (Fig. 5.20c). Multiple hubs are used to fully cover k-space. The hub parameters determine whether the amount of overlap between hubs is less (Fig. 5.20d) or more (Fig. 5.20e).

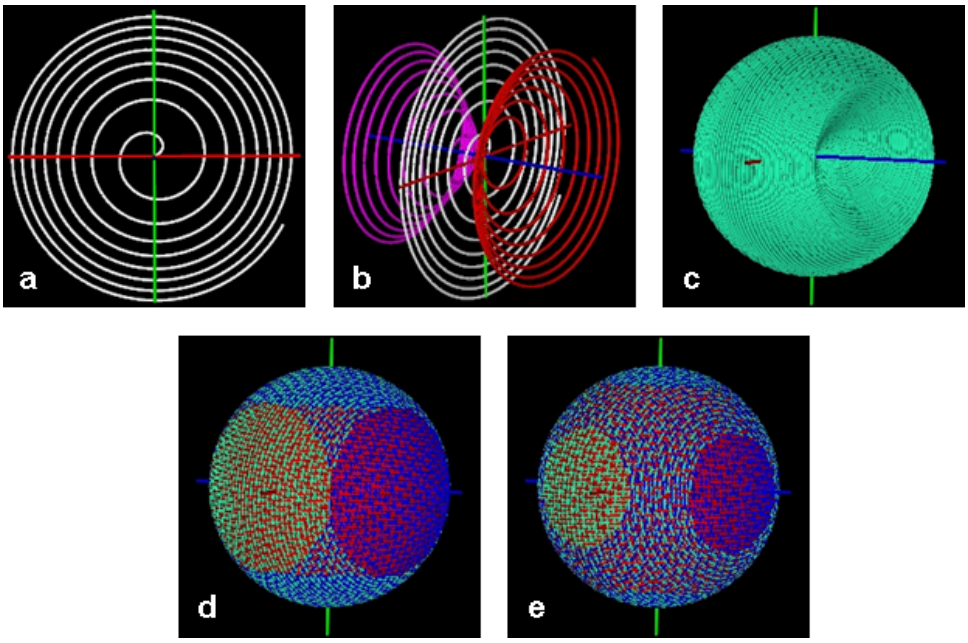

Figure 5.20: The base spiral trajectory used to form the Floret trajectory (a); the base spiral is stretched and rotated (b) to form a hub (c). The hub parameters specify the amount of overlap between the hubs: less (d) or more (e).

Phase Accumulation in k-Space for the Floret Trajectory

Figure 5.21 shows the phase accumulation in k-space for a typical Floret trajectory and constant B_0 in-homogeneity. The phase accumulation along the the three primary axes is also shown in Fig. 5.22. The phase accumulation in k-space due to concomitant fields for a given point is illustrated in Fig. 5.23, and Fig. 5.24 depicts the phase accumulation along the three primary axes. It is evident that the accumulation can be approximated by a 3D quadratic function in both cases, permitting the use of the rapid de-blurring algorithm for both B_0 in-homogeneity and concomitant field correction.

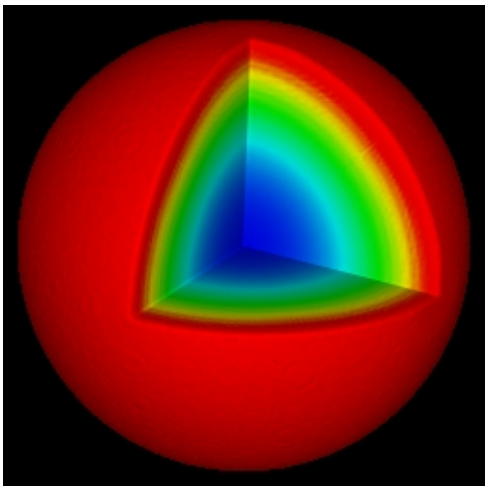

Figure 5.21: The phase accumulation in k-space for a typical Floret trajectory and a constant B_0 off-resonance of 50 Hz.

B_o Map Estimation

B_0 maps can be generated from two data sets collected at different $T_e s$ as the difference in $T_e s$ allows phase accrual, at every pixel, that is proportional to the frequency offset. A weighted average of the estimates from different coils then gives the final estimate of the frequency offset. This procedure can be represented as (56) :

$$\Delta_\omega = \measuredangle \sum_{i=1}^{N} F_i S_i \qquad [5.52]$$

where N is the number of coils, F_i is the complex data of the i-th coil collected at the first T_e value, S_i is the complex data of the i-th coil collected at the second T_e value, and $\measuredangle$ denotes the phase.

B_0 maps can be collected at lower resolution and interpolated (zero-padding in k-space) to the required higher resolution. The accuracy of such maps depends

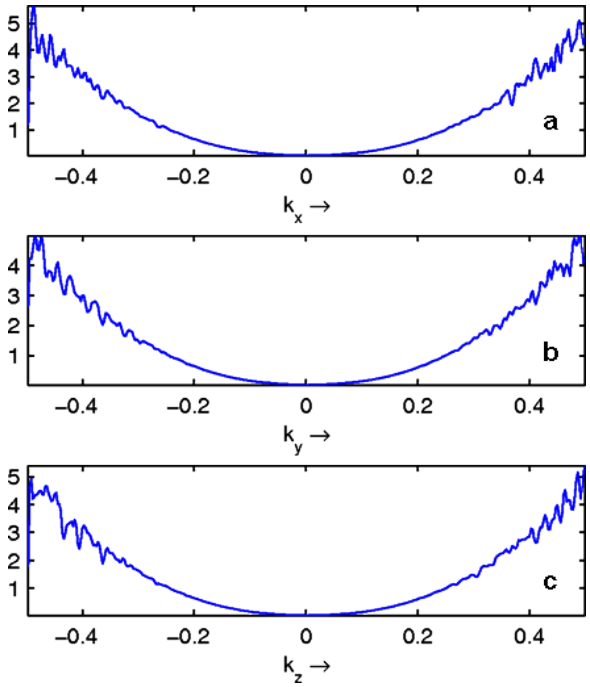

Figure 5.22: Phase accumulation along x-axis (a), y-axis (b) and z-axis (c) for the Floret trajectory and constant B_0 off-resonance in Fig. 5.21.

on the amount of interpolation. To determine the permissible resolution limits, in-vivo data was collected at 1.5 mm resolution and 24 cm FOV. Lower resolution datasets were generated from the collected dataset by progressively excluding high frequency content in k-space. Field maps were then computed from all the datasets. Figure 5.25 plots the RMS difference between the low resolution field maps and the field map at the original resolution. The residual RMS values suggest that field maps can be collected at a resolution that is 0.5mm lower than the target resolution, and Fourier interpolated.

Collecting field map data at a lower resolution helps improve the SNR and keeps

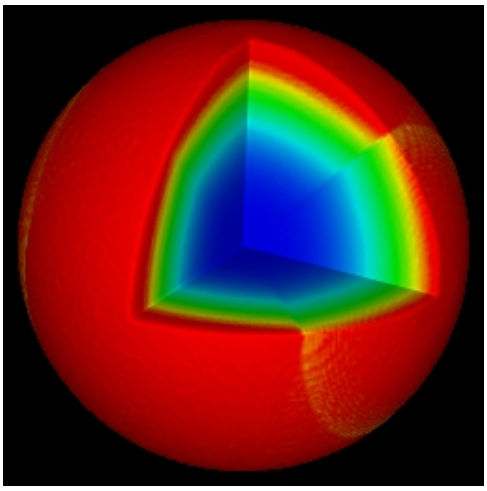

Figure 5.23: The concomitant phase accumulation in k-space for a typical Floret trajectory and pixel location (x = 0 cm; y = 5 cm; z = 5 cm).

the scan time small. The SNR can be further improved by using a TA of 1000 (57) as tissue contrast is not an objective in field map data. These factors together make it possible to generate a high-SNR high-dynamic range using just 2 scans.

The datasets were also filtered in k-space with a Hamming window to achieve a smooth field map (Figs. 5.26d-f). Also, since the Floret trajectory is used to collect the field map datasets, care is necessary to ensure that there is minimal blurring in the field map datasets. This is ensured by limiting the ADC time; ADC times of 1.5 ms or less were found to be sufficient. For the Floret trajectory, ADC times can be limited by using a combination of a high number of spiral interleaves (5000), low resolution (1.5 mm), high gradient magnitude (4 G/cm) and high slew rate (13 G/cm/ms).

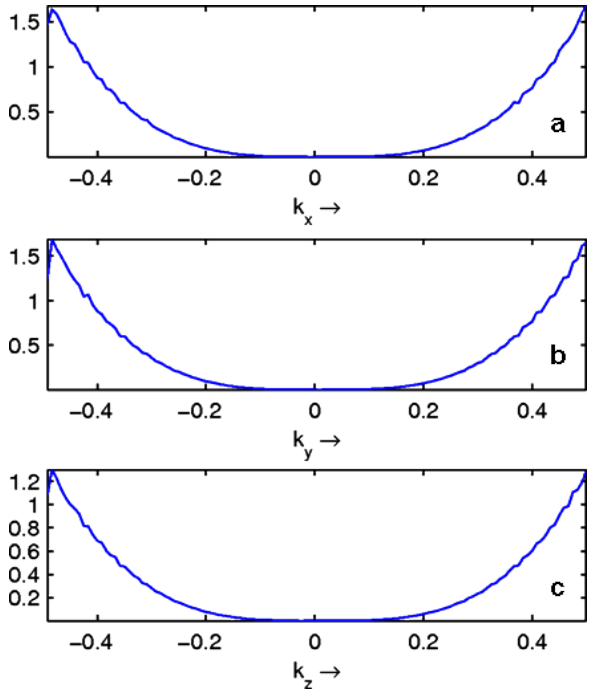

Figure 5.24: Concomitant field phase accumulation along x-axis (a), y-axis (b) and z-axis (c) for the Floret trajectory and pixel location in Fig. 5.23.

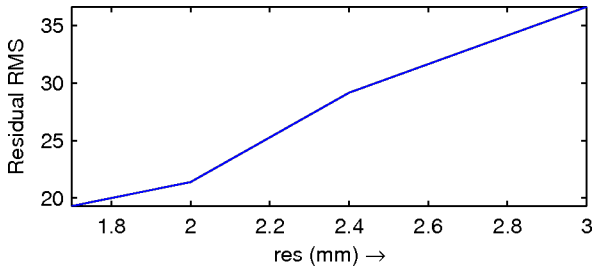

Figure 5.25: RMS values of the difference between the field maps from lower resolution datasets and the field map from the corresponding high resolution (1.5mm) dataset.

Results

In-vivo data was acquired on a 3T GE scanner. The B_0 map data was collected with 24 cm FOV, 1.5 mm resolution, 5000 spiral interleaves, 15 ms T_r, 10 degree

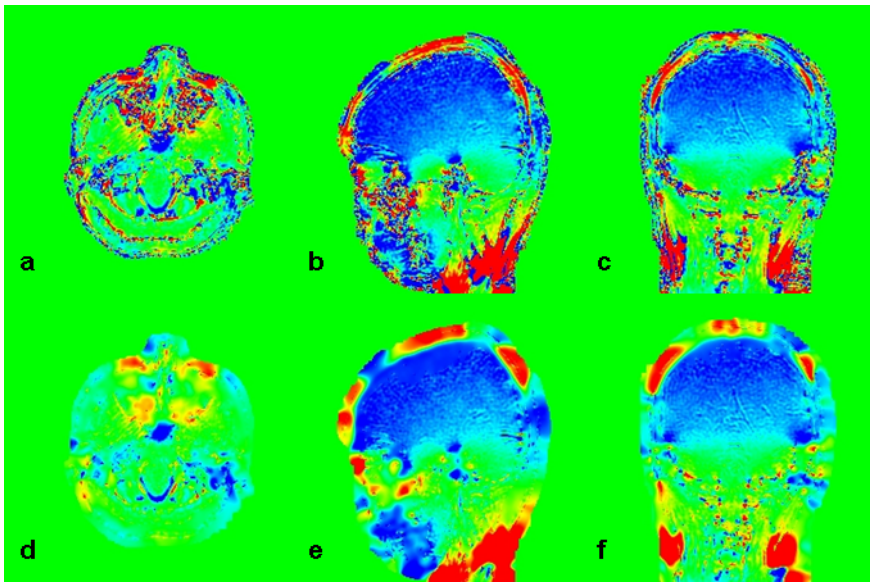

Figure 5.26: Representative axial (a,d), sagittal (b,e) and coronal (c,f) slices showing the smoothing (d-f) by filtering in k-space with a Hamming window. The field maps are displayed on a range of $+200Hz$ (red) and $-200Hz$ (blue).

flip angle and a T_e difference of 0.4 ms. The resulting ADC time was 1.5 ms. The blurred data was collected with 24 cm FOV, 1.0 mm resolution, 3000 spiral interleaves, 18.5 ms T_r, 20 degree flip angle and a T_e difference of 3.4 ms. The resulting ADC time was 6 ms. All acquisitions were collected with fat suppression via spectral spatial RF (8).

The data was first reconstructed with regular gridding and sampling density correction. The B_0 maps and the virtual concomitant field maps were then computed using the approach outlined previously. The blurring correction for both zeroth-order and first-order effects was then carried out using the separable method outlined before. The dataset had a total phase accumulation in k-space of 7.5 cycles

due to B_0 in-homogeneity and 0.5 cycles due to concomitant fields.

The B_0 correction results for representative axial (Fig. 5.27), sagittal (Fig. 5.28) and coronal (Fig. 5.29) slices from the Floret data set are shown. The results are in tune with the collected field map. The residual artifact is due to inaccuracies in the field map. The field map inaccuracy has also introduced some artifact (Fig. 5.28, Fig. 5.29).

The field map inaccuracies are probably due to bad estimates at locations with low signal strength. The efficacy of fat suppression also has a large impact on the field map estimates. Further work to incorporate water-fat separation techniques and field map estimation with more accurate smoothing conditions to account for locations with low signal strength is expected to help achieve improved results.

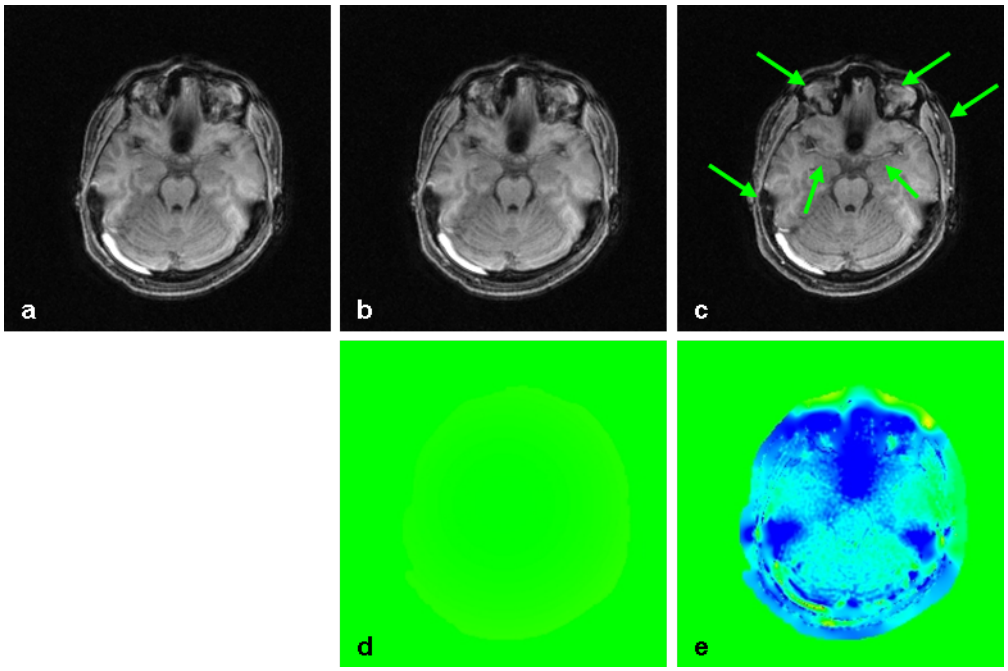

Figure 5.27: A representative axial slice collected using a Floret trajectory (a) and corrected for concomitant (b), B_0 in-homogeneity (c). The green arrows indicate improvement. The associated concomitant map (d) is displayed on a range of $+75Hz$ (red) and $-75Hz$ (blue). The associated B_0 map (e) is displayed on a range of $+200Hz$ (red) and $-200Hz$ (blue). Note that the concomitant map values for this slice are minimal (consistent with Eq. 5.47); hence, the image (d) is all green. Also the B_0 deviations are for the most part negative; hence, the B_0 map (d) is for the most part blue.

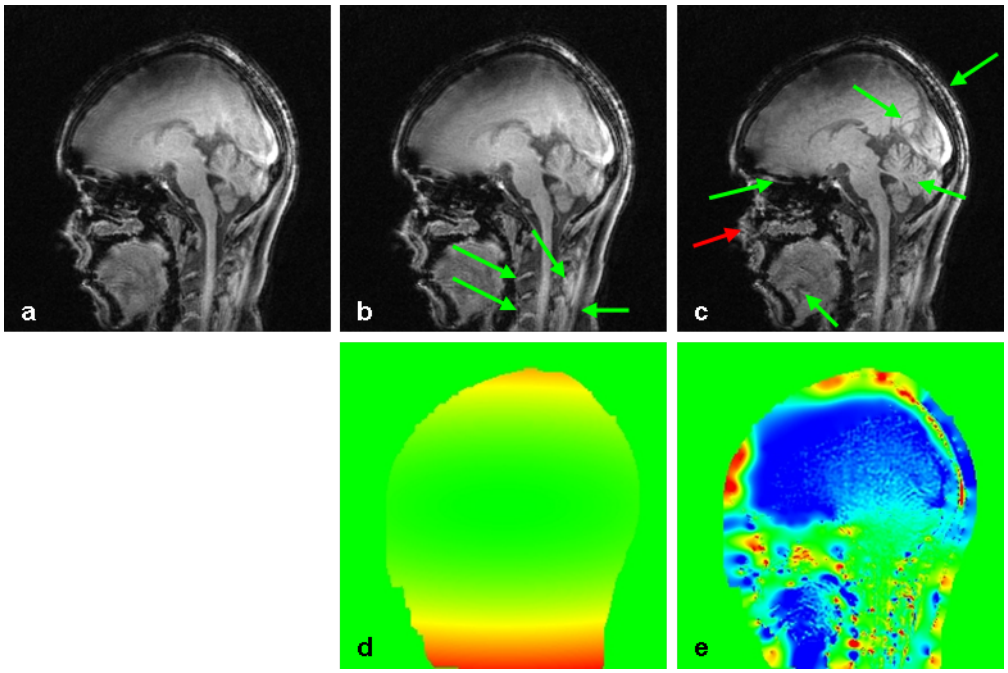

Figure 5.28: A representative sagittal slice collected using a Floret trajectory (a) and corrected for concomitant (b) B_0 in-homogeneity (c). The green and red arrows indicate resulting improvement and distortion, respectively. The associated concomitant map (d) is displayed on a range of $+75Hz$ (red) and $-75Hz$ (blue). The associated B_0 map (e) is displayed on a range of $+200Hz$ (red) and $-200Hz$ (blue).

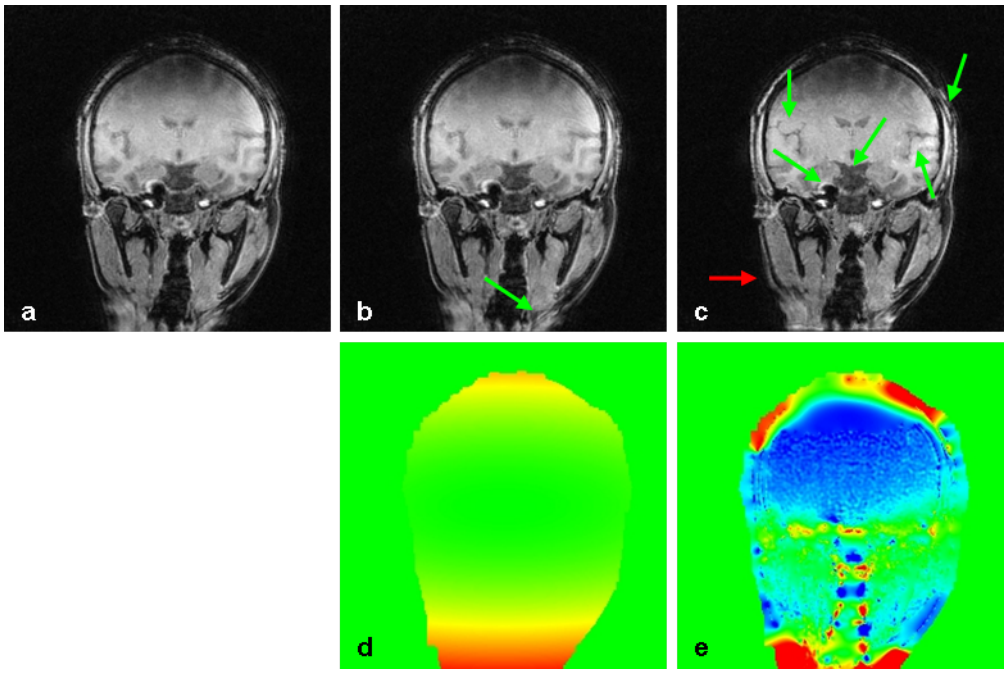

Figure 5.29: A representative coronal slice collected using a Floret trajectory (a) and corrected for concomitant (b), and B_0 in-homogeneity (c). The green and red arrows indicate resulting improvement and distortion, respectively. The associated concomitant map (d) is displayed on a range of $+75Hz$ (red) and $-75Hz$ (blue). The associated B_0 map (e) is displayed on a range of $+200Hz$ (red) and $-200Hz$ (blue).

Chapter 6

CONCLUSION

Practical application of post Cartesian imaging requires efficient trajectory design, accurate knowledge of the trajectory deviations (if any) and reconstruction to handle potential artifacts. This work presents advances in trajectory design (Chapter 3), trajectory estimation (Chapter 4) and improved reconstruction (Chapter 5).

CONTRIBUTIONS

Traditionally, 2-D scans are designed to support an isotropic field-of-view (iFOV). When imaging elongated objects, significant savings in scan time can potentially be achieved by supporting an elliptical field-of-view (eFOV). This work presents an empirical closed form solution to adapt the PROPELLER trajectory for an eFOV. The proposed solution is built on the geometry of the PROPELLER trajectory permitting the scan prescription and data reconstruction to remain largely similar to standard PROPELLER. The proposed solution is validated by experimental results, the point spread function (PSF) depicting the achieved FOV and a comparison of SNR performance to iFOV scans. Details of the possible savings in scan time have also been described.

Conventional trajectory measurements are carried out on single gradient channels. The effect (if any) of playing out waveforms concurrently on multiple gradient channels is generally assumed to be negligible. This work presents a simple

approach to measure this effect on zeroth-order deviations (gradient delays) for spiral waveforms. The proposed method uses a line phantom to generate a uniform structure in k-space. The orientation of the structure is pre-determined via the position of the phantom. This prior information helps in estimating gradient coupling effects (if any).

Spatial encoding for spiral scans is sensitive to B_0 in-homogeneities. The resulting artifact is a spatially varying blur. Due to the nature of the spiral trajectory, the zeroth-order blur effects can be corrected in a computationally efficient manner with separable kernels. This work presents extensions to include first-order and concomitant field correction. The first-order effect is modeled as an unaccounted change in sampling density. The nature of the spiral trajectory is used to derive an analytical expression for the deviation in sampling density on a pixel-by-pixel basis. It is also demonstrated that the trajectory characteristics permit modeling the concomitant field effects as blur due to a static in-homogeneity map. An empirical equation for sufficient kernel length is also derived. The SNR performance of the algorithm is illustrated. Steps to estimate a B_0 field map are also outlined. The algorithm is demonstrated on a 3-D in vivo floret trajectory dataset. These advances are expected to make post Cartesian imaging more accessible for applications in the clinic.

FUTURE WORK

Field map accuracy is one of the prominent factors in achieving good deblurring. Water-fat signal separation has a significant impact on the B_0 map estimation and de-blurring itself. Future work to estimate the B_0 map more accurately will require a water-fat separation algorithm incorporated into it. Locations with low signal strength also contribute to inaccuracies in the estimated field map. Identifying these low signal regions and interpolating the field map in such areas will also help improve the field map accuracy. It is expected that a multi-level deblurring to account for both water and fat signals with accurate field maps from water-fat separated datasets, will help improve deblurring for B_0 and concomitant field artifacts.

REFERENCES

1. Bloch F, Hansen WW, Packard M. Nuclear induction. Phys Rev 1946;70:474–485.

2. Purcell EM, Torrey HC, Pound RV. Resonance absorption by nuclear magnetic moments in a solid. Phys Rev 1946;69:37–38.

3. Lauterbur PC. Image formation by induced local interactions: Examples employing nuclear magnetic resonance. Nature 1973;242:190–191.

4. Kumar A, Welti D, Ernst RR. NMR Fourier zeugmatography. J Magn Reson 1975;18:69–83.

5. Mansfield P. Multi-planar image formation using NMR spin echoes. J Phys C 1977;C 10:L55 – L58.

6. Levitt MH. Spin dynamics: Basics of nuclear magnetic resonance. Wiley, 2007.

7. Liang ZP, Lauterbur PC. Principles of magnetic resonance imaging: A signal processing perspective. IEEE Press, 1999.

8. Bernstein MA, King KF, Zhou XJ. Handbook of MRI Pulse Sequences. Elsevier, 2004.

9. Pipe JP. Basic spin physics. Clin N Am 1999;7:607–627.

10. Nishimura DG. Principles of Magnetic Resonance Imaging. 1996.

11. Hu X, Parrish T. Reduction of field of view for dynamic imaging. Magn Reson Med 1994;31:691–694.

12. Yao L, Cao Y, Levin DN. 2D locally focused MRI: Applications to dynamic and spectroscopic imaging. Magn Reson Med 1996;36:834–846.

13. Scheffler K. Tomographic imaging with nonuniform angular sampling. J Comput Assist Tomogr 1999;23:162–166.

14. Larson PEZ, Gurney PT, Nishimura DG. Anisotropic field-of-views in radial imaging. IEEE Trans Med Imaging 2008;27:47–57.

15. King KF. Spiral scanning with anisotropic field of view. Magn Reson Med 1998;39:448–456.

16. Larson PEZ, Lustig MS, Nishimura DG. Anisotropic field-of-view shapes for improved PROPELLER imaging. Magn Reson Imaging 2009;27:470–479.

17. Pipe JG. Motion correction with PROPELLER MRI: Application to head motion and free-breathing cardiac imaging. Mag Reson Med 1999;42:963–969.

18. Ramanujan S. Modular equations and approximations to π. Quart J Math (Oxford) 1914;45:350–372.

19. Robison RK, Pipe JG. Analysis and refinement of PROPELLER MRI motion correction [abstract]. In Proceedings of the International Society of Magnetic Resonance in Medicine. Berlin, 2007; 1731.

20. Jackson JI, Meyer CH, Nishimura DG. Selections of a convolution function for Fourier inversion using gridding. IEEE Trans Med Imaging 1991;10:473–478.

21. Pipe JG, Menon P. Sampling density compensation in MRI: Rationale and an iterative numerical solution. Mag Reson Med 1999;41:179–186.

22. Firebank MJ, Coulthard A, Harrison RM, Williams ED. A comparison of two methods for measuring the signal to noise ration on MR images. Phys Med Biol 1999;44:N261–N264.

23. Alley MT, Glover GH, Pelc NJ. Gradient characterization using a Fourier-transform technique. Magn Reson Med 1998;39:581–587.

24. Mason GF, Harshbarger T, Hetherington HP, Zhang Y, Pohost GM, Twieg DB. A method to measure arbitrary k-space trajectories for rapid MR imaging. Mag Res Med 1997;38:492–496.

25. Papadakis NG, Wilkinson AA, Carpenter TA, Hall LD. A general method for measurement of the time integral of variant magnetic field gradients: applications to 2D spiral imaging. Mag res Med 1997;15:567–578.

26. Takahashi A, Peters T. Compensation of multi-dimensional selective excitation pulses using measured k-space trajectories. Magn Reson Med 1995;34:446–456.

27. Robison RK, Devaraj A, Pipe JG. Fast, simple gradient delay estimation for spiral MRI. Mag Res Med 2010;63:1683–1690.

28. Yudilevich E, Stark H. Spiral sampling in magnetic resonance imaging – The effects of in-homogeneities. IEEE Transactions on Medical Imaging 1987;MI-6:337–345.

29. Park HW, Kim YH, Cho ZH. Fast gradient-echo chemical-shift imaging. Magnetic Resonance in Medicine 1988;7:340–345.

30. Schneider E, Glover G. Rapid in vivo proton shimming. Magn Reson Med 1991;18:335–347.

31. Webb P, Macovski A. Rapid, fully automatic, arbitrary-volume in vivo shimming. Magn Reson Med 1991;20:113–122.

32. Sepponen RE. A method for imaging of chemical shift or magnetic field distributions. Magnetic Resonance in Imaging 1985;3:163–167.

33. Sekihara K, Kohno H, Matsui S. A new method of measuring static field distribution using modified Fourier imaging. Journal of Physics E: Scientific Instruments 1985;18:224–227.

34. Maeda A, Sano K, Yokoyama T. Reconstruction by weighted correlation for

MRI with time-varying gradients. IEEE Transactions on Medical Imaging 1988;7:26–31.

35. Shenberg I, Macovski A. In-homogeneity and multiple dimension considerations in magnetic resonance imaging with time-varying gradients. IEEE Transactions on Medical Imaging 1985;MI-4:165–174.

36. Hutchison JMS, Sutherland RJ, Mallard JR. NMR imaging: Image recovery under magnetic fields with large non-uniformities. J Phys E: Sci Instrum 1978; 11:217–221.

37. Sekihara K, Kohno H, Matsui S. Image restoration from non-uniform magnetic field influence for direct Fourier NMR imaging. Physics in Medicine and Biology 1984;29:15–24.

38. Sekihara K, Kohno H. Image restoration from non-uniform static field influence in modified echo planar imaging. Medical Physics 1987;14:1087–1089.

39. Lai CM. Reconstructing NMR images under magnetic fields with large inhomogeneities. Journal of Physics E: Scientific Instruments 1982;15:1093–1100.

40. Donnell MO, Edelstein WA. NMR imaging in the presence of magnetic field in-homogeneities and gradient field in-homogeneities. Medical Physics 1985; 12:20–26.

41. Chang H, Fitzpatrick M. A technique for accurate magnetic resonance imaging in the presence of field in-homogeneities. IEEE Transactions on Medical Imaging 1992;11:319–329.

42. Noll DC, Meyer CH, Pauly JM, Nishimura DG, Macovski A. A homogeneity correction method for magnetic resonance imaging with time-varying gradients. IEEE Transactions on Medical Imaging 1991;10:629–637.

43. Kadah YM, Hu X. Simulated phase evolution rewinding (SPHERE): A technique for reducing B_0 in-homogeneity effects in MR images. Magn Reson Med

1997;38:615–627.

44. Noll DC, Pauly JM, Meyer CH, Nishimura DG, Macovski A. De-blurring for non-2D fourier transform magnetic resonance imaging. Magnetic Resonance in Medicine 1992;25:319–333.

45. Man LC, Pauly JM, Macovski A. Improved automatic off-resonance correction without a field map in spiral imaging. Magnetic Resonance in Medicine 1997; 37:906–913.

46. Moriguchi H, Dale BM, Lewin JS, Duerk JL. Block regional off-resonance correction (BRORC): A fast and effective de-blurring method for spiral imaging. Magnetic Resonance in Medicine 2003;50:643–648.

47. Man LC, Pauly JM, Macovski A. Multi-frequency interpolation for fast off-resonance correction. Magnetic Resonance in Medicine 1997;37:785–792.

48. Schomberg H. Off-resonance correction of MR images. IEEE Transactions on Medical Imaging 1999;18:481–495.

49. Ahunbay E, Pipe JG. Rapid method for de-blurring spiral MR images. Magn Reson Med 2000;44:491–494.

50. Pruessmann KP. Limits of SNR and practical consequences [abstract]. In Annual Meeting of the International Society of Magnetic Resonance in Medicine, Weekend Tutorials. Seattle, 2006; .

51. Noll DC, Fessler JA, Sutton BP. Conjugate phase MRI reconstruction with spatially variant sample density correction. IEEE Transactions on Medical Imaging 2005;24:325–336.

52. Abramowitz M, Stegun IA. Handbook of Mathematical Functions with formulas, graphs, and Mathematical Tables. Dover, 1970.

53. Bernstein MA, Zhou XJ, Polzin JA, King KF, Ganin A, Pelc NJ, Glover GH. Concomitant gradient terms in phase contrast MR. Magn Reson Med 1998;

39:300–308.

54. King KF, Ganin A, Zhou XJ, Bernstein MA. Concomitant gradient field effects in spiral scans. Magn Reson Med 1999;41:103–112.

55. Pipe JG, Robison RK, Devaraj A, Zwart N, Johnson KO. A fast 3D trajectory with orthogonal over-sampling [abstract]. In Proceedings of the International Society of Magnetic Resonance in Medicine. Stockholm, 2010; 4974.

56. Lu K, Liu TT, Bydder M. Optimal phase difference reconstruction: Comparison of two methods. Mag Res Imag 2008;26:142–145.

57. Pipe JG, Robison RK. Simplified signal equations for spoiled gradient echo MRI [abstract]. In Proceedings of the International Society of Magnetic Resonance in Medicine. Stockholm, 2010; 3114.